



In-situ trace element and Sr isotope signature of apatite: A new key to unravelling the genesis of polymetallic mineralisation in black shales of the Early Cambrian Niutitang Formation, Southern China

Sophie Decrée^{a,*}, Jan Pašava^b, Jean-Marc Baele^c, Julien Mercadier^d, Delia Rösel^e, Hartwig Frimmel^f

^a Royal Belgian Institute of Natural Sciences-Geological Survey of Belgium, Brussels, Belgium

^b Czech Geological Survey, Prague, Czech Republic

^c Department of Geology and Applied Geology, University of Mons, Mons, Belgium

^d Université de Lorraine, CNRS, CREGU, GeoRessources Lab, Vandoeuvre-lès-Nancy, France

^e Department of Earth Sciences, University of Göteborg, Göteborg, Sweden

^f Bavarian Georesources Centre, Dept. of Geodynamics and Geomaterials Research, Institute of Geography and Geology, University of Würzburg, Germany

ARTICLE INFO

Keywords:

Phosphorite
Ni-Mo-PGE sulphide ore
Rare Earth Elements
Mafic affinity
Hydrothermal brines

ABSTRACT

The Early Cambrian Mo-Ni-PGE sulphidic black shale in the Niutitang Formation on the margin of the Yangtze Craton (Southern China) is known for its extremely high metal concentrations. It is also very rich in phosphate that formed contemporaneously with the sulphides. Detailed petrological as well as in-situ trace element and Sr isotope analyses of authigenic apatite revealed new information on the metallogensis of this enigmatic rock unit. In the ore bed, apatite forms nodules or is found in phosphatic (phosphoclasts) and sulphide clasts. In the latter, the replacement of organic matter and sulphides by apatite microspherules suggests a microbially mediated phosphogenesis. Enrichment in middle rare earth elements emphasizes the role played by Fe-oxyhydroxides and organic matter in element scavenging. Moderately reducing conditions are supported by a lack of Ce and Eu anomalies. The trace element signature of apatite and its initial $^{87}\text{Sr}/^{86}\text{Sr}$ (0.7032–0.7190), which is - for a group of analyses - well below the signature of Lower Cambrian seawater, points to some contribution from mafic rock-sourced hydrothermal brines. This effectively explains the exceptional enrichment of Ni and PGE in the sulphides. Seawater remains, however, the preferred source for other elements such as P and Mo.

1. Introduction

The polymetallic Mo-Ni-PGE sulphide and phosphate-rich bed within the black shale unit of the Lower Cambrian Niutitang Formation (Huangjiawan mine, Zunyi region, northern part of the Guizhou Province, Southern China) is well-known for its extreme metal concentrations (e.g. Chen et al., 1982; Coveney and Chen, 1991; Fan, 1983; Han et al., 2015; Jiang et al., 2006; Lehmann et al., 2007; Li et al., 2013; Mao et al., 2002; Pašava et al., 2008, 2013, 2017; Xu et al., 2013). For instance, Mo and Ni are enriched over 1000 times compared to the average continental crust (with at least 4 wt% Mo and 2 wt% Ni) and Au-Pt-Pd contents in the ore bed reach 100 times the average content in this reservoir (1–249 ppm of precious metals, including Au, Pt, Pd, and Os)

(e.g. Fan, 1983; Mao et al., 2002; Pašava et al., 2008, 2013, 2017). The metalliferous black shale occurs along a belt extending about 1600 km across South China (Steiner et al., 2001). The ore bed mostly contains sulphides and phosphate as mineralised clasts. The latter have been interpreted to represent remnants of a shallow-water hardground horizon rich in metals, which was reworked, transported (at least over short distances) and re-deposited in the deeper part of the basin (e.g. Murawchick et al., 1994; Pašava et al., 2008).

A lot of effort has been made to identify the source of the metals and to understand the complex genesis of the mineralisation in the Niutitang ore bed. As a general assumption, the timing of the mineralisation is syndimentary to early diagenetic (e.g. Orberger et al., 2005; Pašava et al., 2008), and sulphides and phosphate replaced organic material,

* Corresponding author.

E-mail addresses: sophie.decree@naturalsciences.be (S. Decrée), jan.pasava@geology.cz (J. Pašava), jean-marc.baele@umons.ac.be (J.-M. Baele), julien.mercadier@univ-lorraine.fr (J. Mercadier), delia.rosel@gu.se (D. Rösel), hartwig.frimmel@uni-wuerzburg.de (H. Frimmel).

<https://doi.org/10.1016/j.oregeorev.2022.105130>

Received 26 October 2021; Received in revised form 3 September 2022; Accepted 26 September 2022

Available online 27 September 2022

0169-1368/© 2022 The Authors. Published by Elsevier B.V. This is an open access article under the CC BY-NC-ND license (<http://creativecommons.org/licenses/by-nc-nd/4.0/>).

likely through the mediation of bacteria and algae (e.g. Křibek et al., 2007; Murowchick et al., 1994; Orberger et al., 2007).

Nevertheless, two contrasting views have been expressed regarding the source of the metals and enrichment processes. The first model favours derivation of all the metals that are concentrated in the Niutitang ore bed from seawater. Based on Mo, Cr and Hg isotope data, Lehmann et al. (2007, 2016), Xu et al. (2012, 2013) and Yin et al. (2017) suggested metal scavenging from seawater through redox/oxidative changes, sorption and/or uptake by biomass, with the metals being supplied by oxidative weathering of the continental crust. A dominant seawater origin of the metals found further support by the Re-Os isotopic signature of the ore (Fu et al., 2016; Lehmann et al., 2003; Mao et al., 2002; Xu et al., 2011) and a detailed geochemical study (Pagès et al., 2018). The alternative model considers hydrothermal fluids as a major, or at least additional, contributor of the metals in the Niutitang ore bed. This model explains the observed abnormal contents of Ni and PGE in the ore bed and various metal ratios (e.g. relative to Mo or total organic carbon) that are not seawater-like (e.g. Emsbo et al., 2005; Han et al., 2017, 2020; Jia et al., 2018; Jiang et al., 2007; Křibek et al., 2007; Liu et al., 2015; Lott et al., 1999; Murowchick et al., 1994; Orberger et al., 2007; Pašava et al., 2010, 2019; Pi et al., 2013; Steiner et al., 2001). A study focusing on Ni isotope ratios further suggested that the observed light $\delta^{60}\text{Ni}$ signature of the ore bed is best explained by an external source of Ni that would have been derived from weathering of mafic/ultramafic rocks in the hinterland (Pašava et al., 2019). Recently, new Cu and Zn isotope data, coupled with previously published Cd, Cr, Ni, Mo, Hg and Se isotope data, led to a hybrid model, in which parts of the polymetallic metal enrichment is likely related to hydrothermal input along the rifted margin of the Yangtze Platform (Lehmann et al., 2022).

In the context of this debate, a detailed study of apatite can add helpful information. Apatite is commonly considered a resistant mineral, retaining its primary geochemical signature, and it is thus suitable to fingerprint the processes leading to its formation (e.g. Baele et al., 2019; Belousova et al., 2002; Bouzari et al., 2016; Bruand et al., 2016;

Kempe and Gotze, 2002). In the sedimentary environment, the study of apatite chemistry can provide clues about element sources and depositional/early diagenetic conditions (e.g. McArthur and Walsh, 1984; Shields and Stille, 2001; Kidder et al., 2003; Zhu et al., 2014; Chen et al., 2015; Alvaro et al., 2016).

Such studies were performed on various phosphate-rich beds hosted by Neoproterozoic to early Cambrian sedimentary rocks of the Yangtze Craton. Among these, trace element and Sr-Nd isotope data obtained on phosphatic rocks of the Neoproterozoic (Ediacaran) Doushantuo Formation point to a crustal/detrital source for the REE, phosphogenesis in an anoxic environment and distribution of the REE modified by diagenetic fluids (Xin et al., 2015, 2016). Further petrological observations and oxygen isotope data on phosphate nodules confirmed the diagenetic timing of alteration (Ling et al., 2004). An in-situ investigation on the phosphate concretions highlighted an even more complex diagenetic history of the phosphatic grains, with several sources for the REE that include hydrothermal contribution (Zhu and Jiang, 2017).

Recent trace element studies were also conducted on large phosphate nodules in the Lower Cambrian phosphorite beds in the Yangtze Craton, including those of the Niutitang Formation (in the areas of Daotuo, Jinsha, Longbizui, Rongxi, Sansha and Songtao; Fig. 1). Depending on the site investigated, the REE signature is either more seawater-like (Ye et al., 2020) or highlights exchange with pore water at an early stage of apatite precipitation (Ye et al., 2021) and during early diagenesis (Ye et al., 2020). Differences in terms of Nd isotopic compositions between the two types would reflect a change in the REE source from a seawater-dominated pore water to diagenetic fluid-dominated pore waters (Zhu et al., 2014). Such an evolution of the REE source was also observed in single phosphate nodules from other early Cambrian formations (Mufu Mountain of Nanjing; Jiang et al., 2007). Several trace element studies also point to an influence of hydrothermal fluids at the time of phosphogenesis, which is commonly evidenced by a positive Eu anomaly (Gao et al., 2018; Ye et al., 2020, 2021; Zhu et al., 2014).

Despite the general interest in phosphate beds of the Neoproterozoic-

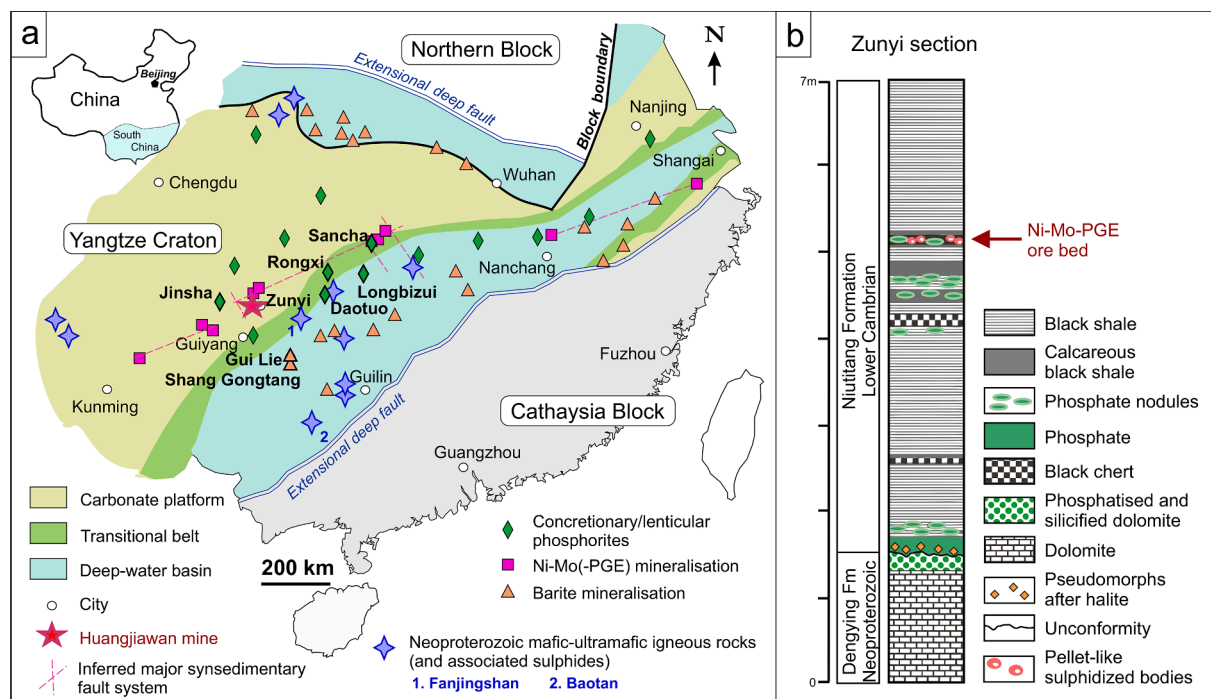


Fig. 1. (a) Sketch paleogeographic map of the Yangtze Craton during the Upper Neoproterozoic/Lower Cambrian (modified after Chen et al., 2009; Gao et al., 2018; Steiner et al., 2001; Zhu et al., 2014), with the distribution of concretionary/lenticular phosphorites (Gao et al., 2018; Ye et al., 2020, 2021; Zhu et al., 2014), barite mineralisation (Pašava et al., 2008; Ye et al., 2020), Ni-Mo(-PGE) mineralisation (Pašava et al., 2008; Steiner et al., 2001), inferred major synsedimentary fault system (Steiner et al., 2001) and Neoproterozoic mafic-ultramafic igneous rocks (Huang and Wang, 2019; Zhou et al., 2017); (b) Stratigraphic position of the Niutitang Formation in the Zunyi region, modified after Pašava et al., (2008).

Lower Cambrian interval of the Yangtze Craton, no attention has been paid to the phosphate nodules that are intimately – spatially and temporally – associated with polymetallic sulphides in the Niutitang ore bed. Yet, this apatite provides essential information about the possible source(s) of the elements constituting the deposit (seawater, detrital components, hydrothermal fluids) and processes involved in P and metal concentration in the system. To fill this gap was the aim of this study, which was achieved through a detailed investigation of apatite in the ore bed in the Niutitang Formation at the Huangjiawan mine (Zunyi region). This investigation is based on a petrographic characterisation including cathodoluminescence (CL), in-situ chemical and isotopic analyses using laser ablation-inductively coupled-plasma mass-spectrometry (LA-ICP-MS) to quantify the chemical composition (trace elements) in apatite and determine its Sr isotope composition (as performed previously by Decrée et al., 2020; Emo et al., 2018; Gillespie et al., 2021; Li et al., 2018; Ravindran et al., 2019; Yang et al., 2018; Ying et al., 2020; Zeng et al., 2016; Zhao et al., 2015). The combined analyses broaden the field of application of in-situ isotope geochemistry in sedimentary apatite.

2. Geologic setting

Neoproterozoic to Early Cambrian strata of the Yangtze Craton (China) host numerous phosphorite beds. In most of these beds, the size of the phosphate nodules can reach a few centimeters (Gao et al., 2018; Ye et al., 2020, 2021; Zhu et al., 2014). The Niutitang Formation is also known for its exceptionally rich polymetallic Mo-Ni-PGE sulphide ore bed (e.g. Murowchick et al., 1994; Lott et al., 1999; Steiner et al., 2001; Mao et al., 2002; Emsbo et al., 2005; Jiang et al., 2007; Lehmann et al., 2007; Orberger et al., 2007; Pašava et al., 2008;). Several black shale-hosted ore deposits occur in restricted areas along a 1600 km belt and are probably linked to a major deep fault zone parallel to a former island arc system at the southern margin of the Yangtze platform (Steiner et al., 2001).

The Yangtze Craton is a composite craton that is mainly made up of a Precambrian basement and Neoproterozoic to Palaeozoic cover. It was shaped by continental rifting (Wang and Li, 2003), accompanied by volcanic and plutonic activity (Gao et al., 1995). The Neoproterozoic (Ediacaran) and Lower Cambrian sediment deposition was controlled by the northeast-trending Nanhua rift-type basin, which is bounded by several large-scale structural faults (Li 1986). These sediments significantly vary laterally from siliciclastic-dominated series overlying the Cathaysia Craton to a carbonate-siliciclastic succession in the Yangtze Craton (Chen et al., 2018). Three main Ediacaran to Early Cambrian sedimentation domains have been distinguished (Steiner et al., 2007; Zhu et al., 2014): (i) a carbonate platform, where phosphatic black shale was deposited under evaporitic conditions in shallow water lagoons, (ii) a transitional belt reflecting an environment comparable to recent continental margins, and (iii) deep basin. Black shale was accumulated in the deeper parts of more restricted basins formed during the sag phase (Li, 1986; Gao et al., 1995; Wang and Li, 2003).

The depositional environment of the Niutitang Formation corresponded to the transition from an oxidic shallow shelf to an anoxic deep shelf (Li, 1986). Its age was constrained using various methods. Among the obtained ages, Pb-Pb isochrons on black shale and mixed sulphides from the ore bed led to data of 531 ± 24 Ma and 521 ± 54 Ma, respectively (Chen et al., 2003; Jiang et al., 2007). These ages overlap a Re-Os isochron ages for the black shale and the sulphide assemblage of 537 ± 10 Ma and 535 ± 11 Ma, respectively (Jiang et al., 2003, 2007). Other composite Re-Os isochrons on mixed sulphides from the ore bed provided ages of 541 ± 16 Ma (Mao et al., 2002) and 521 ± 5 Ma (Xu et al., 2011). The most precise constraint on the age of the ore bed and host shale is a SHRIMP U–Pb age of 532.3 ± 0.7 Ma obtained on a zircon hosted in a volcanic ash bed in the lowermost part of the Niutitang Formation (Jiang et al., 2009).

In the area of the Huangjiawan mine (Fig. 1), the Niutitang Formation rests unconformably on dolomite of the Neoproterozoic (Ediacaran)

Dengying Formation. There, the Dengying Formation is strongly phosphatised and silicified. The basal part of the Niutitang Formation is made up of an intercalation of brownish phosphates, dolomite and chert lenses. These are considered as transgressive shallow water sediments (Zeng, 1998) that were deposited in a marine environment with high salinity (Pašava et al., 2008). The phosphorite gradually evolves towards black shale (comprising carbonates, phyllosilicates, and organic-rich laminae) alternating with phosphate and chert layers. These sediments were also deposited in a highly saline environment (Frimmel and Spangenberg 2007).

The ore bed is approximately 20 cm thick and occurs 3–5 m above the base of the Niutitang Formation (Fig. 1). Its contact with the underlying black shale is sharp, whereas large, scattered sulphide clasts occur between the ore bed and the overlying black shale (Pašava et al., 2008). The ore bed is mainly composed of a variety of clasts - ranging from a few mm up to 1 cm in size - that constitute 70 to 85 vol% of the rock and testify of (short distance) transport of some of the mineralised material to a deeper environment (Murowchick et al., 1994). Most of the clasts are sulphide pellets exhibiting a concentric fabric that comprises a repetition of pyrite, organic matter and a mixed-layer phase composed of Mo, C, S (Murowchick et al., 1994; Kao et al., 2001; Křibek et al., 2007; Orberger et al., 2007; Pašava et al., 2008). Other clasts are made up of (i) large rounded to angular fragments of structureless phosphate nodules, (ii) concentric/radial phosphate ooids and (iii) fragments of Ni-Fe sulphides and Mo–C–S phases (Pašava et al., 2008). In the ore bed, PGE are bound to pyrite and Ni-sulphides (Pašava et al., 2013, 2017). The matrix of the ore bed is highly porous and consists of silicates, carbonates and organic matter (Křibek et al., 2007; Orberger et al., 2007). Sediment compaction is reflected by flattening and coalescence of the clasts. Deformation led to an overprint of the primary sedimentary textures, which makes the distinction between clasts and diagenetic nodules difficult (Pašava et al., 2008).

Previous studies led to commonly accepted ideas about the genesis of the deposit, which are summarized hereafter. Textural relationships and microthermometric studies of the alteration and gangue minerals support the hypothesis of a syndepositional to early diagenetic ore deposition at elevated temperature (>200 °C) (Lott et al., 1999; Pašava et al., 2004; Orberger et al., 2005). The involvement of bacteria/algae is also likely, considering the concentric fabric of the sulphide pellets (named clasts, hereafter) and the phosphate ooid size and shape (e.g. Steiner et al., 2001; Murowchick et al., 1994; Křibek et al., 2007; Pašava et al., 2008). The mineralised bed has been interpreted as a phosphate- and sulphide-rich subaquatic hardground (e.g. Murowchick et al., 1994; Křibek et al., 2007; Pašava et al., 2008), formed during a period with very low input of terrigenous material (Murowchick et al., 1994; Steiner et al., 2001). Formation of the mineralised layer would have occurred at moderate depth, close to the oxic–anoxic and sulphide-saturated water interface. This assumption is based on the likely presence of phototrophic coccoid cyanobacteria (Steiner et al., 2001; Křibek et al., 2007), in an agitated shallow-water shelf environment (Murowchick et al., 1994; Pašava et al., 2008).

3. Material and methods

Four samples from the Mo-Ni-PGE ore bed in the Huangjiawan mine area (Fig. 1a) were selected and studied for their petrography and chemical composition. Petrographic analysis was performed using a Quanta 20 ESEM-FEI scanning electron microscope (SEM facilities at the Royal Belgian Institute of Natural Sciences). The SEM is equipped with an energy-dispersive spectrometer (Apollo 10 Silicon Drift EDS detector; EDAX). Cathodoluminescence (CL) analysis was performed at the University of Mons using a cold-cathode CL system operated at 15 kV beam voltage and 500 µA current (Cambridge Image Technology Limited, model Mk5). The surface of the unfocused electron beam on the sample was 12 × 4 mm, resulting in a current density of about 10 µA/mm². CL spectra were recorded with a CITL optical spectrometer model OSA2

making possible to acquire from 350 to 1100 nm at 3.7 nm spectral resolution. Spectra were acquired and processed using the Spectragryph optical spectroscopy software (<https://www.effemm2.de/spec-tragryph/>).

Quantitative microanalyses of major element concentrations (Electronic Supplementary Material, Item 3) were acquired using a JEOL JXA 8800L electron microprobe at the Institute of Geography and Geology, University of Würzburg (Germany). It was operated at 15 kV and 20 nA, with a beam diameter of 10 μm . This microprobe is equipped with four wavelength-dispersive (WDS) spectrometers and standard LDE1, TAP, PET and LIF crystals (LiF for F, Fe_2O_3 for Fe, SrSO_4 for Sr). Mineral standards (vanadinite for Cl, apatite for P and Ca, and andradite for Si) supplied by CAMECA (SX Geo-Standards) were used for reference. The $\text{L}\alpha$ line was used for the measurements of Sr and Ba, and the $\text{K}\alpha$ line for all other elements. The lower limit of detection is typically better than 0.05 wt%. For each mineral spot, the relatively mobile element F was analysed first to prevent its potential loss during the analysis.

Laser-ablation inductively-coupled mass-spectrometry (LA-ICP-MS) was used to obtain the trace element concentrations of apatite. The analytical focus was on detecting rare earth elements. LA-ICP-MS analyses were performed at GeoRessources (Nancy, France), with a GeoLas excimer laser (ArF, 193 nm, Microlas) coupled with a conventional transmitted and reflected light microscope (Olympus BX51) for sample observation and laser beam focusing and an Agilent 8900 triple quadrupole ICP-MS used in no-gas mode. The external standard was NIST SRM 610 (Jochum et al., 2011) and ^{44}Ca was used as internal standard. NIST SRM 614 and NIST SRM 612 silicate glasses were analysed and considered as cross-calibration samples to control the quality of the analyses (precision, accuracy, repeatability) and to correct for possible drift during the analytical session for concentrations of the NIST silicate glasses. Information about the quality of the secondary standards is provided in the Electronic Supplementary Material (Item 1). Calcium concentrations constrained by EMPA from the same apatite grains were used to calculate the concentrations of the other elements measured. Two different Ca concentrations, in weight percent, were used for internal standardization: 40.04 based on electron microprobe analyses on pure apatite and 27.4 based on EDS analyses of an assemblage comprising apatite-quartz-sulphide. In these zones, the minerals are mixed at micrometre scale and REE, Y and Sr are taken to be hosted only by apatite. Indeed, the contents of these elements in micas and sulphides are commonly very low and negligible compared to their concentration in apatite (e.g. Tillberg et al., 2019; Villaseca et al., 2020; Zeng et al., 2015; Zhao et al., 2021). The precisions were better than 10 % (rel.) for all REE. Data treatment was done using the software “Iolite” (Paton et al., 2011), following Longerich et al. (1996) for data reduction. More information is provided in the Electronic Supplementary Material (Item 1).

The methodology for Sr isotope analysis is presented in Electronic Supplementary Material, Item 6. A summary of the method is provided here, the extended method is part of the Electronic Supplementary material, Item 1. The Sr isotope composition from the apatite grains was measured at the Microgeochemistry Facility, Department of Earth Sciences, University of Gothenburg. There, an ESI 213 NWR laser ablation system is coupled to an Agilent 8800 ICP-QQQ (see details in Zack and Hogmalm (2016) and Hogmalm et al. (2017)). Data were collected during four analytical sessions. Circular laser spots with different diameters were used during individual runs. A repetition rate of 10 Hz was used for all runs and the fluence varied between 5.9 and 7.3 J/cm^2 . Helium was used as carrier gas and mixed with nitrogen before introduction into the ICP-MS/MS; N_2O was used as reaction gas and introduced overnight into the reaction chamber prior to analyses. Additional He was supplied during two of the four analytical sessions.

NIST SRM 610 was used as primary reference material for the calculation of the $^{87}\text{Sr}/^{86}\text{Sr}$ ratios and BCR-2G to test accuracy, precision and reproducibility between the analytical sessions. The preferred $^{87}\text{Sr}/^{86}\text{Sr}$ ratios for both reference materials are 0.709699 ± 0.000018

(2 s) (Woodhead and Hergt 2001) and 0.705003 ± 0.000008 (2 s) (Elburg et al., 2005), respectively. The $^{87}\text{Rb}/^{86}\text{Sr}$ ratios were calculated using BCR-2G as primary reference material to correct for mass bias and drift. Initial $^{87}\text{Sr}/^{86}\text{Sr}$ ratios were modelled based on the constrained $^{87}\text{Sr}/^{86}\text{Sr}$ and $^{87}\text{Rb}/^{86}\text{Sr}$ ratios and an assumed age of 532 Ma (Jiang et al., 2009).

4. Results

4.1. Petrography

The investigated ore bed is a mineralised dolomitic shale that consists mostly of dolomite, white mica, quartz, and organic matter (OM). It hosts numerous variably flattened nodules of sulphides that are up to 0.5 cm in length and 1 to 2 mm in thickness. These were referred to as pellets in the literature, although they are actually clasts (e.g. Murowchick et al., 1994; Kr̄fbek et al., 2007; Pašava et al., 2008), which are variably brecciated/fractured (Fig. 2a). The dolomitic matrix is made of rhombic-shaped crystals that show a zoned texture under cathodoluminescence (CL), with a brownish dull-luminescent core surrounded by bright red euhedral overgrowths (see insert in Fig. 2a). The red luminescence of dolomite is typically related to Mn^{2+} -activation, whereas its quenching (leading to brown-dull CL) is commonly related to the presence of Fe^{2+} (e.g. Marshall 1988; Hiatt and Pufahl 2014).

In the ore bed, apatite exhibits distinct morphological varieties. The first morphotype is sub-rounded to sub-angular nodules (Apn for apatite nodules in Fig. 2), which commonly reach a few hundred micrometres in width (Fig. 2b-f). They consist of closely-packed clusters of tiny prismatic apatite crystals with a size of about 5 to 10 μm . These nodules commonly contain inclusions of silicates (quartz, white mica), dolomite and sulphides (pyrite and gersdorffite; Fig. 2f). Note that dolomite rhombohedra of the matrix are locally embedded at the edge of the nodules (white arrows in Fig. 2d). Apatite nodules typically exhibit a violet colour under CL (Fig. 2d), which is due to REE activation (e.g. Marshall, 1988; Blanc et al., 2000; Kempe and Götze 2002; Mitchell et al., 1997, 2014, 2020), mostly Sm^{3+} , Eu^{2+} and Dy^{3+} (as illustrated in CL spectra; Electronic Supplementary Material, Item 2). A weaker activation (darker CL) can be observed in the core of the nodules (Fig. 2d), which is also characterised by a lower porosity and inclusion content (Fig. 2c). Similar blue-violet-luminescent apatite is also found as overgrowth around bright green-luminescent grains of apatite (Apg for apatite grain in Fig. 2g), which are abundant in the ore bed as detrital grains together with detrital quartz and zircon. The yellow-green CL of apatite is usually ascribed to Mn^{2+} activation and is common in detrital, granite-derived apatite grains (e.g. Roeder et al., 1987; Marshall 1988; Kempe and Götze 2002). The blue-violet-luminescent overgrowths are themselves commonly brecciated.

The second apatite morphotype (Aps and ApsS for apatite spherules in phosphatic clasts and in sulphide clasts, respectively, Figs. 2 and 3) consists of microspherules of uniform size (2–4 μm in diameter) that form closely-packed aggregates in phosphatic (Fig. 2h,i) and sulphide clasts (Fig. 3a,b). These spherules are embedded in an interstitial violet CL apatite matrix (indicated by “Ac” in Fig. 2i and Fig. 3a), which fills the remaining porosity in association with OM. In phosphatic clasts (Fig. 2h,i), apatite spherules constitute a kind of mosaic together with small grains of mica and quartz. Apatite spherules contain a nucleus of phyllosilicate, carbonate and/or OM. A vague layering in the spherules is defined by thin, porous layers. Finally, a lining of OM is observed as spherule coating and in the remaining voids. Though being roughly rounded, the shape of the spherules is conditioned by the other spherules that grew at the same time in the vicinity. In sulphide clasts (Fig. 3a-b), well-rounded apatite spherules are densely packed and form “patches” in association with a Mo—C—S phase (as described by Kao et al. (2001) and Pašava et al. (2008), for instance; Fig. 3a), pyrite and small detrital phyllosilicate grains. Most apatite spherules appear homogeneous. In others, apatite is admixed with a Mo—C—S phase that is incompletely

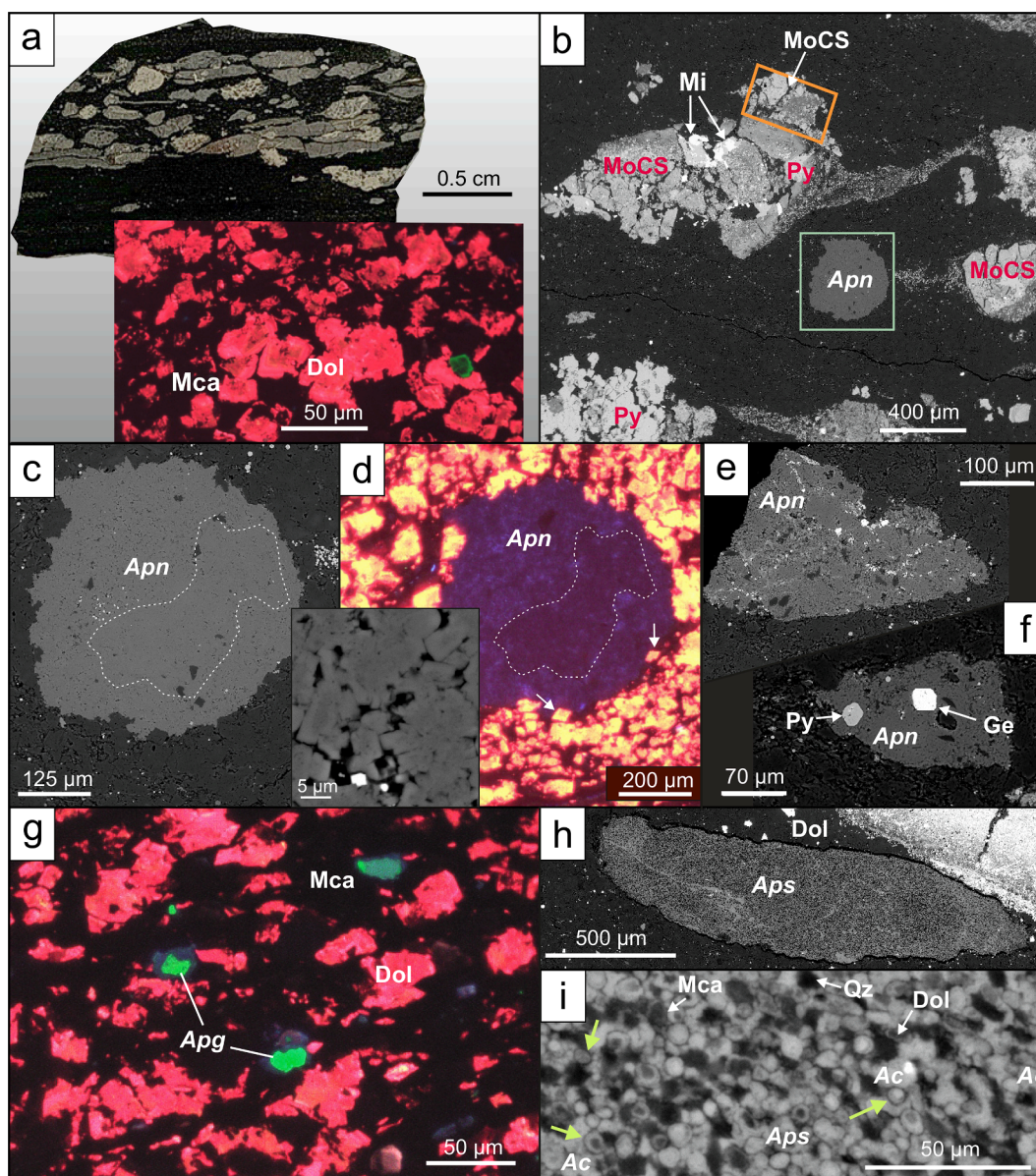


Fig. 2. Selected macrophotograph (a), cathodoluminescence (CL) (insert in a, d, g) and backscattered electron (b, e, g, h) photomicrographs of the Ni-Mo-PGE phosphatic ore bed of the Niutitang Formation; mineral abbreviations: Ac-apatite inter-spherule cement (Type 2), Apg- apatite grains (Type 1), Apn-apatite nodules (Type 2), Aps-apatite spherule zone in phosphatic clasts (Type 2), Dol-dolomite, Ge-gersdorffite, Mca-mica, Mi-millerite, MoCS- C and MoS₂ mixed-layer phase, Qz-quartz, Py-pyrite. (a) General view of the ore bed with sulphide and phosphatic nodules/clasts; the insert shows the red-luminescent dolomite matrix; (b) Brecciated sulphide clast and phosphate nodule (which is presented in Fig. 2c,d); the orange rectangle indicates the zone showed in Fig. 3d-f; (c-d) Detailed view on a violet-luminescent apatite nodule, the centre of which is characterised by a more compact and less luminescent zone. The insert shows the internal texture of the nodule, which is made of prismatic crystals. Note the dolomite rhomboedra enclosed in apatite at the rim of the nodule (white arrows, sample BSC1-grain1). Exposure time was increased to capture the weak apatite luminescence, which resulted in a yellow luminescence colour for the adjacent dolomite due to over-exposition; (e-f) Subangular phosphate nodules enclosing subhedral to euhedral Fe and Ni sulphides (sample BSC1-grain2&3); (g) Brecciated/corroded apatite grains exhibiting a complex luminescence texture with a detrital/inherited green-luminescent core overgrown by blue-violet-luminescent apatite; (h-i) Closely-packed apatite spherules in a phosphatic clast. The spherules develop around a nucleus made of phyllosilicates or carbonates. The green arrows indicate linings of organic matter. Apatite also forms an inter-spherules cement (Ac) (sample PC1-Zone2).

replaced by phosphate. The latter exhibits annular textures that could possibly represent relicts of former microspherules (Fig. 3a). In sulphide clasts, the layered apatite spherules underline the concentric fabric (Fig. 2b, 3b-c). Later deposition of gersdorffite, millerite and sphalerite is locally evident at sulphide clast margins (Fig. 2b and Fig. 3a,b).

Lastly (as the third morphotype, Apr for apatite replacement in Fig. 3), a dull-violet-luminescent apatite is observed as pervasive replacement of pyrite, Mo—C—S and OM in sulphide clasts (Fig. 3d-g). The invasion pattern is quite complex, as illustrated in Fig. 3e-g. This phosphatisation seemingly did not extend beyond the clast's boundary.

A thin alternation of apatite and gersdorffite as grain coating suggests that both minerals formed contemporaneously (Fig. 3d).

Based on the above observations, three apatite types can be distinguished: The first one (Type 1) is represented by the bright green luminescing grains that are scattered in the dolomitic shale (for apatite grain in Fig. 2g). This apatite type is very rare compared to the other types. The second apatite type (Type 2) is characterised by violet CL and occurs in the form of nodules (Apn for apatite nodules in Fig. 2), spherules in phosphatic clasts and overgrowths around the Type 1 apatite (Aps for apatite spherules in phosphatic clasts Fig. 2h,i and Ac for

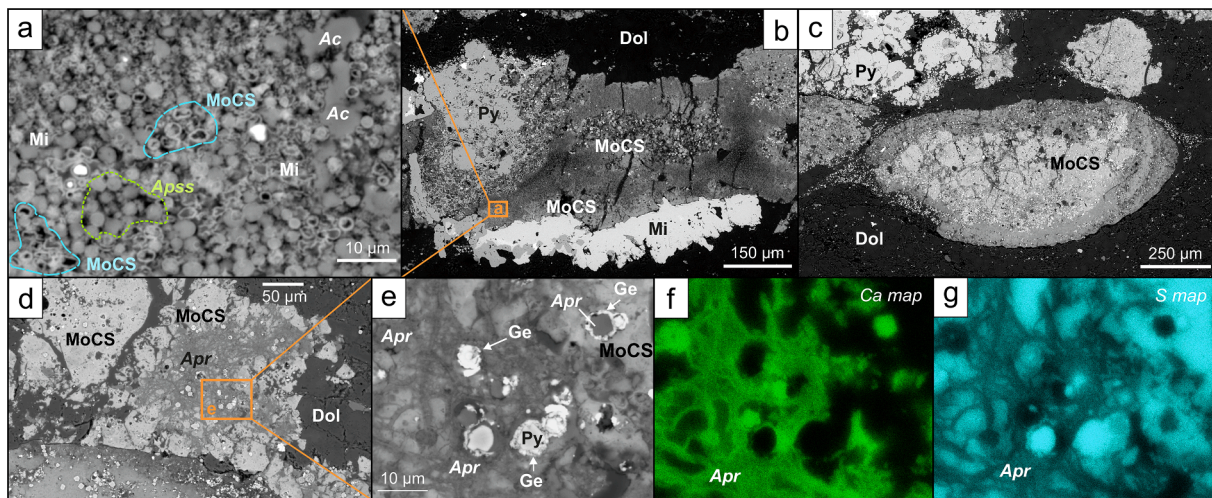


Fig. 3. Backscattered electron photomicrographs of the of the Ni-Mo-PGE phosphatic ore bed of the Niutitang Formation; Ac-apatite inter-spherule cement (Type 2), Apr-apatite as pervasive replacement of sulphides-OM (Type 3), Apsps-apatite spherule zone in sulphide clasts (Type 3), Dol-dolomite, Ge-gersdorffite, Mi-millerite, MoCS- C and MoS₂ mixed-layer phase, Py-pyrite. (a) Apatite spherules (as emphasized by the dashed green line) replace MoCS spherulitic/annular textures (as those highlighted by the dashed blue line) in a sulphide clast. Apatite is also present as inter-spherule cement. Millerite occasionally fills the porosity (sample BSC1-Zone7); (b) Enlarged view of the same sulphide clast, in which one can see alternating pyrite and MoCS (associated with apatite) before millerite deposition (sample BSC1-Zone7); (c) Concentric fabric in a rounded sulphide clast (sample PC1); (d-g) Apatite as pervasive replacement of early formed sulphide (likely MoCS) before gersdorffite deposition. EDS element maps for Ca and S, showing the replacement pattern of sulphides by apatite (sample BSC1-Zone1b).

apatite inter-spherule cement in Fig. 2i and Fig. 3a). This apatite is seemingly coeval with sulphides. By contrast, a third type of apatite (Type 3) that is also violet-luminescent is replacing sulphides and sulphide-OM mixture in sulphide clasts, either as microspherules (Apsps in Fig. 3) or as pervasive replacement (Apr in Fig. 3).

4.2. Mineral chemistry

The three apatite types displaying different CL colours also differ systematically in their mineral chemistry. The P₂O₅ content is higher in the green-luminescent apatite (Type 1): 40.82–41.8 wt% (Electronic Supplementary Material, Item 3) and lower in the violet-luminescent apatite associated with sulphides (Type 2 and Type 3): 30.01–32.83 wt%. The range of CaO and F content is moderate in both types: 55.52–57.06 wt% CaO and 3.53–5.08 wt% F. Most of the F contents obtained by EMPA are above the theoretical maximum in apatite of 3.73 %. This could be due to grain orientation and anisotropic ion diffusion, which are known to cause overestimation of F as measured with the electron microprobe (e.g. Goldoff et al., 2012; Stormer et al., 1993), but could also be explained by a substitution mechanism (see below). In all apatite types, SiO₂ contents are moderate to high, varying from 0.10 to 1.16 wt%. The SrO contents range from 0.05 to 0.22 wt%, whereas Cl content is very low (<0.05 wt%).

Raman spectroscopy provides complementary information about apatite chemistry (see Electronic Supplementary Material, Item 4). Compared to a reference fluorapatite (here, the green-luminescent detrital apatite grains), the violet-luminescent apatite associated with the sulphide mineralisation (Type 2 and Type 3) showed (i) a shift towards lower wavenumbers in the range characteristic of the ν_1 vibration mode (at $\sim 965\text{ cm}^{-1}$) and (ii) a decrease of the peak intensity in the range of the ν_2 and ν_4 vibration mode (between 400 and 650 cm^{-1}). Both alterations of the apatite Raman spectra suggest partial replacement of PO₄³⁻ by CO₃²⁻ (Penel et al., 1998). The PO₄³⁻-CO₃²⁻ substitution typically induces an excess of fluorine in apatite (McClellan and Van Kauwenbergh 1991), which is observed in Type 2 and Type 3 apatite. This substitution would also explain the low P₂O₅ contents of the violet-luminescent apatite, which can therefore be regarded as carbonate-fluorapatite (CFA).

Compared to the post-Archaeon Australian shale composite (PAAS),

the violet-luminescent apatite is enriched in REE (LA-ICP-MS analyses; Electronic Supplementary Material, Item 5). The total REE content is higher in spherulitic and sulphide-replacement apatite (Type 3) (2783 < ΣREE < 4081 ppm) than in nodular apatite (Type 2) (1105 < ΣREE < 2203 ppm). Enrichment in the MREE is indicated by the conspicuous bell shape of the PAAS-normalized REE patterns of violet-luminescent apatite. These patterns also show enrichment in LREE compared to HREE (Fig. 4a), with (La/Yb)_{Norm.PAAS} ratios varying from 1.40 to 2.48. In addition, they are characterised by a very slight (if any) negative Ce anomaly (0.89 < Ce/Ce*_{Norm.PAAS} < 1.04) and no or only a slight positive Eu anomaly (0.97 < Eu/Eu*_{Norm.PAAS} < 1.14). On the other hand, the Type 1 green-luminescent apatite exhibits a rather flat PAAS-normalised REE pattern (Fig. 4a; $\Sigma\text{REE} = 272$ and 278 ppm), with a slight enrichment in MREE and HREE ((La/Yb)_{Norm.PAAS} = 0.38 and 0.45), a slight negative anomaly in Ce (Ce/Ce*_{Norm.PAAS} = 0.82 and 0.88) and virtually no Eu anomaly (Eu/Eu*_{Norm.PAAS} = 1.02 and 1.08). The chondrite-normalised REE patterns (Fig. 4b) show a different shape with a marked enrichment in LREE (12.8 < (La/Yb)_{Norm.Chond} < 22.7 for the violet CL apatite (Type 2 and Type 3) as opposed to (La/Yb)_{Norm.Chond} = 3.5 and 4.1 for the Type 1 green CL apatite), no Ce anomaly and a negative Eu anomaly (Eu/Eu*_{Norm.Chond} varying from 0.64 and 0.71 for all apatite types). Whereas REE content and distribution are quite consistent for the same apatite type, their Y, Sr and Rb contents can vary significantly. They are overall lower in apatite nodules (Type 2) (341 < Y < 687 ppm, 980 < Sr < 1905 ppm, 1.2 < Rb < 17.8 ppm) than in apatite spherules in sulphides and in apatite replacing sulphides and OM (Type 3) (634 < Y < 1198 ppm, 1584 < Sr < 2432 ppm, 8.6 < Rb < 39 ppm).

In comparison with the REE content of apatite from the ore bed, the REE signatures (bulk and LA-ICP-MS analyses) obtained on large apatite nodules from the Niutitang Formation outside of the ore bed - show overall the same kind of PAAS-normalised pattern (with a MREE bulge), though less enrichment in (L)REE (157 < ΣREE < 1125 ppm; 0.19 < (La/Yb)_{Norm.PAAS} < 1.26). These patterns exhibit pronounced negative anomalies in Ce (0.36 < Ce/Ce*_{norm.PAAS} < 0.70) and typically slight positive anomalies in Eu (0.92 < Eu/Eu*_{norm.PAAS} < 2.17, with an average value of 1.28) (Zhu et al., 2014; Gao et al., 2018; Ye et al., 2020,2021).

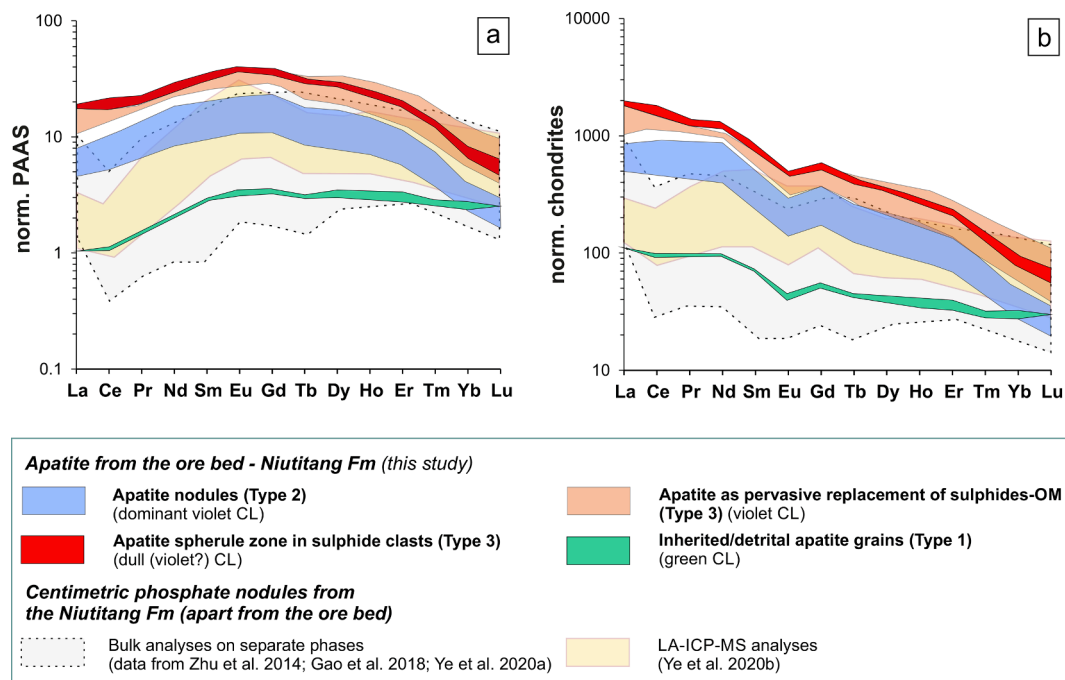


Fig. 4. REE patterns of apatite in the ore bed of the Niutitang Formation (LA-ICP-MS analyses). Apatite types/generations are referred as (Type 1), (Type 2) and (Type 3) (see text for further explanation). REE patterns are normalized to the Post Archaean Australian Shales (PAAS; Condie 1993) (a) and to the chondrites (values from McDonough and Sun 1995) (b). Bulk analyses and LA-ICP-MS analyses obtained on other phosphate nodules from the Niutitang Formation are given for comparison.

4.3. Sr isotope composition

Boxplots of Sr isotope data for apatite from the Niutitang ore bed are presented in Fig. 5a (for data see Electronic Supplementary Material, Item 6). The initial isotope ratio ($^{87}\text{Sr}/^{86}\text{Sr}_i$) varies significantly. The least radiogenic $^{87}\text{Sr}/^{86}\text{Sr}_i$ was obtained on Type 2 violet-CL apatite nodules. In this group, the $^{87}\text{Sr}/^{86}\text{Sr}$ ratios range mostly from 0.7032 ± 0.0020 (2σ) to 0.7086 ± 0.0033 (BSC1-Grain1&2). In contrast, Type 2 apatite from two nodules, richer in inclusions, show more radiogenic ratios from 0.7083 ± 0.0060 to 0.7190 ± 0.0092 (PC1-Zone3 and PC2-Zone1). Apatite spherules in phosphatic clasts (Type 2) yielded initial ratios in the same wide compositional range, with $^{87}\text{Sr}/^{86}\text{Sr}_i$ varying from 0.7065 ± 0.0062 to 0.7157 ± 0.0046 (PC1-Zone2). A closer look at these data reveals an effect induced by the size of the analysed zone (two spot sizes at 20 and 100 μm) on the $^{87}\text{Sr}/^{86}\text{Sr}_i$ ratio (Fig. 5b). The latter is more radiogenic and shows less variability when the ablated zone is larger ($0.7130 \pm 0.0029 < \text{Sr}_{(i)} < 0.7155 \pm 0.0022$). Consistently, it is less radiogenic but more variable when the ablated zone is smaller ($0.7065 \pm 0.0062 < \text{Sr}_{(i)} < 0.7157 \pm 0.0046$).

The $^{87}\text{Sr}/^{86}\text{Sr}_i$ of Type 2 apatite spherules from sulphide clasts also varies significantly from 0.7020 ± 0.0024 to 0.7155 ± 0.0056 , an abnormal low value of 0.6986 being discarded (PC1-Zone4 and PC2-Zone2). A similar range of values was obtained on Type 3 apatite occurring as pervasive replacement of sulphides and OM in sulphide clasts. Its $^{87}\text{Sr}/^{86}\text{Sr}_i$ ratios are between 0.7034 ± 0.0062 and 0.7132 ± 0.0049 , depending on the zone investigated (PC1-Zone1, PC2-Zone3, PC3-Zone1).

5. Discussion

5.1. Textural features

Our mineralogical and petrological investigation of phosphates in the ore bed of the Niutitang Formation makes it possible to discriminate three types of apatite. Apatite of the first type, that is characterised by a distinct bright green CL (Apg in Fig. 2g), is considered detrital,

analogous to zircon and quartz grains in the same matrix. The second and third types of apatite display a rather uniform violet CL and a common geochemical signature. Type 2 apatite is considered to be coeval with sulphide phosphatisation (nodules and spherules in phosphatic clasts/nodules, referred as Apn and Aps, respectively, in Fig. 2), whereas Type 3 apatite is considered to be younger (replacement of sulphides and sulphide/OM in sulphide clasts, as spherules (Aps) or pervasive replacement (Apr) in Fig. 3). Although exhibiting distinct morphotypes, the common features shared by Type 2 and Type 3 apatite suggest that they formed during the same phosphogenetic episode and can be considered as authigenic/syngenetic.

5.1.1. Formation and diagenesis of the apatite nodules

The violet-luminescent apatite nodules consist of a fine-grained groundmass of aggregating prismatic crystals. They contain inclusions of minerals that are different to those found dominantly in the host rock (i.e. silicate and sulphide inclusions in the nodules vs dolomite cement; Fig. 2c-f), suggesting that these nodules originate from another depositional environment. Moreover, the structureless, rounded to sub-angular nodules (Fig. 2e,f), by textural evidence, did not form in-situ and could be regarded as phosliothoclasts, by analogy with carbonates (Trappe 2006). Similar blue-violet-luminescent apatite overgrowths that coat detrital apatite grains are also partly brecciated/dismantled (Fig. 2g), reinforcing the hypothesis of mechanical transport of this apatite type, at least over short distances.

Another notable feature is the occurrence of dolomite rhombohedra – forming most of the host rock matrix – embedded at the rim of apatite nodules (Fig. 2d). These bright red-luminescent euhedral dolomite crystals could represent overgrowth linkage and pore lining, likely during deformation/compaction of the sediment (e.g. Hiatt and Pufahl 2014; Choquette and Hiatt 2008). Therefore, their inclusion into apatite nodules would suggest that the latter experienced some diagenetic recrystallization (after their transport to the ore bed). Similarly, the variation in terms of porosity and inclusion content of the nodule (as illustrated in Fig. 2c,d), which is accompanied by a slight change of CL, could have been induced by compaction/diagenesis. However, the

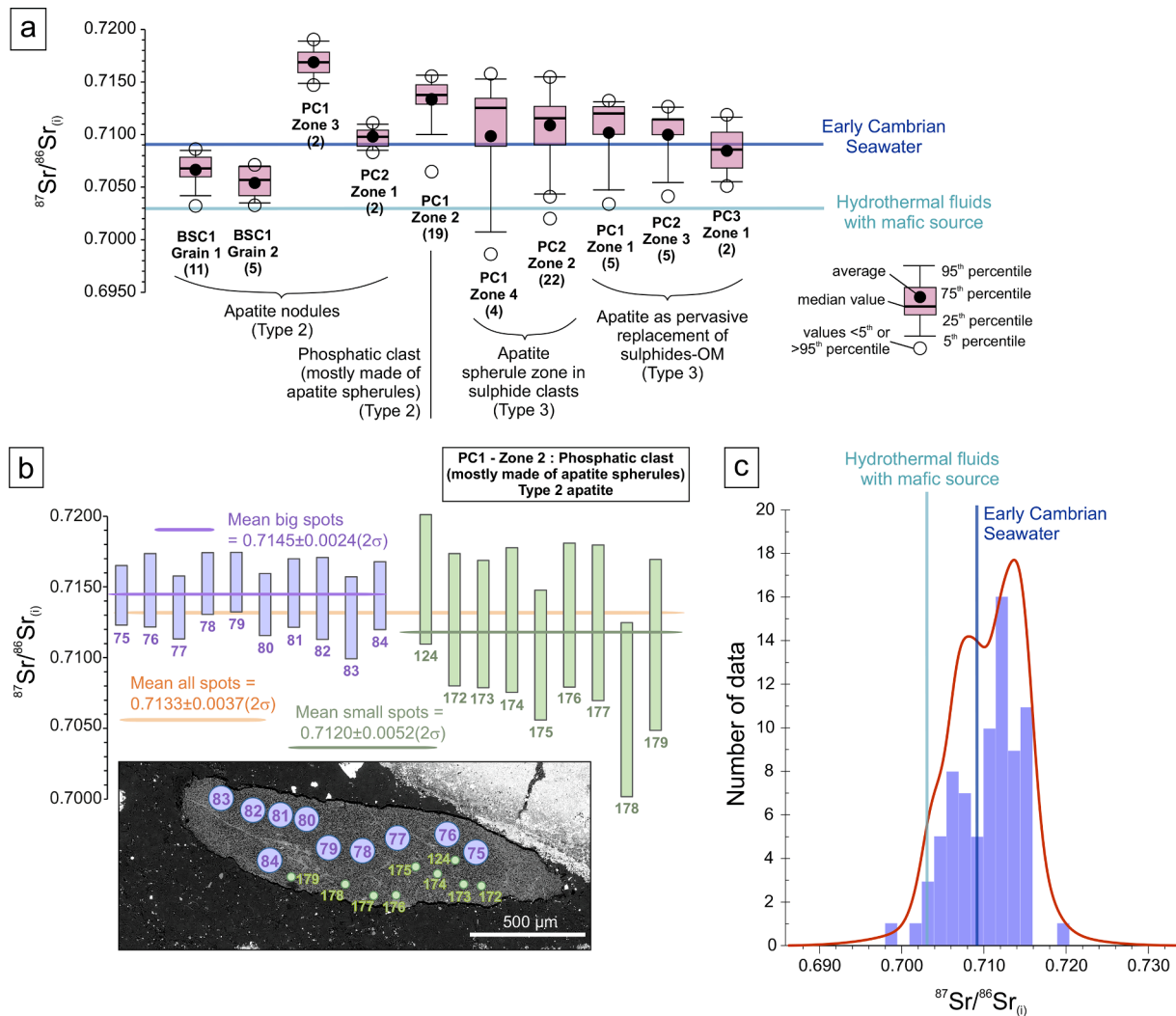


Fig. 5. (a) Box plots showing in-situ $^{87}\text{Sr}/^{86}\text{Sr}_{(t)}$ (LA-ICP-MS analyses) for apatite hosted in the ore bed of the Niutitang Formation. Apatite types/generations are referred as (Type 2) and (Type 3) (see text for further explanation). The number between brackets represents the number of analyses. Early Cambrian seawater Sr isotope composition are from Burke et al., (1982), Veizer et al., (1999) and Hannisdal and Peters (2011) and Sr isotope ratio for hydrothermal fluids with mafic composition are from Von Damm (1990) and Jarvis et al., (1994); (b) in-situ $^{87}\text{Sr}/^{86}\text{Sr}_{(t)}$ (LA-ICP-MS analyses) for apatite hosted in a phosphatic clast (PC1-Zone 2; Type 2). Note the larger variability of the small spot (20 μm) analyses compared to the data obtained when ablating larger areas (big spots, 100 μm). Box height is 2 σ ; (c) Diagram illustrating the frequency distribution for the Sr initial ratios.

pristine shape of the crystallites constituting the nodule suggests that alteration after diagenesis was limited (Yang et al., 2019). This is further supported by the CFA mineralogy of apatite inferred here based on chemistry and Raman spectroscopy. More intense diagenesis/compaction would have undoubtedly resulted in the transformation of CFA towards more stable fluorapatite (McArthur 1985; McClellan and Van Kauwenbergh 1991; Jarvis 1994). These processes also had limited (if any) effect on the trace element distribution in the apatite, as attested by the absence of significant variations in terms of REE content and distribution between the zones of variable porosity in the nodules (i.e. violet CL vs dark CL REE patterns in Fig. 4a,b).

5.1.2. Microspherulitic habit and microbial influence

Another typical feature of apatite is the microspherulitic habit that is encountered in the phosphatic and sulphide clasts. In the former, the Type 2 apatite spherules grew around silicate/carbonate nuclei. They form a mosaic/pavement texture resulting from the replacement of the OM, which progressively led to the concentration of the OM at the boundary of the spherules (Fig. 2i). In the sulphide clasts, Type 3 apatite mostly replaced an early Mo—C—S phase, generally keeping the

globular/annular morphology of the early formed sulphides (Fig. 3a). The micrometric spherule textures of phosphates have been previously ascribed to microbial forms resembling cyanobacteria (e.g. Křibek et al., 2007; Pašava et al., 2008). Microbial phosphate precipitation is very common and produces nucleated or coated grains, resembling those formed in the ore bed. It takes place in depositional environments characterised by low net sedimentation rates (Trappe 2006), which was likely the case at the time of spherule formation (e.g. Murowchick et al., 1994; Steiner et al., 2001; Křibek et al., 2007). Bacterial involvement is further supported by the thin layers of higher porosity that emphasize a vague layering in the spherules. These could have resulted from the dissolution of microbial mat remnants during or after apatite precipitation (Jacquemin 2020). Note that the apatite cement that commonly fills the remaining porosity in spherule-rich zones indicates phosphate supersaturation of the pore water and rapid mineralisation (Wilby et al., 1996).

5.1.3. Relationship with the sulphides

As described above, Type 3 apatite commonly occurs as replacement of OM and a Mo—C—S phase to form microspherules in phosphatic and

sulphide nodules. It is worth mentioning that contrasting observations were made by Pašava et al. (2008), who also noted the replacement of phosphates by sulphides in the clasts. However, these observations are not irreconcilable considering the alternating deposition of sulphides and phosphates in the mineralising system, as described by Murowchick et al. (1994). Textural evidence presented in this study further emphasizes the intimate spatial and temporal association of phosphate and sulphide precipitation, such as the thin alternations of apatite and sulphides that are frequently observed and the fact that apatite and sulphides can be found as replacement of each other. Sulphide precipitation and replacement by apatite might have taken place repeatedly within the same environment over the time interval of rock formation. Besides, the lack of significant phosphatisation or sulphide deposition on the outer surface of the clasts confirms that both processes mostly occurred prior to reworking of the nodules, as previously concluded by several authors (e.g. Murowchick et al., 1994; Steiner et al., 2001; Pašava et al., 2008).

5.2. REE signature and depositional conditions

The REE distribution in apatite has proven to be a helpful tool to understand depositional conditions and subsequent early diagenesis of sedimentary phosphate deposits. REE can serve as proxy of ancient pore water chemistry and, to some extent, of ancient seawater through the examination of their shale-normalized REE patterns and Ce and Eu anomalies (e.g. McArthur and Walsh, 1984; Shields and Stille 2001; Kidder et al., 2003; Zhu et al., 2014; Chen et al., 2015; Alvaro et al., 2016).

Apart from Type 1 detrital apatite, all violet-luminescent apatite of Type 2 and Type 3 from the ore bed share common geochemical features: a PAAS-normalized REE pattern enriched in MREE and a lack of significant Ce and Eu anomalies. MREE enrichment is a common feature of phosphorites associated with Lower-Middle Palaeozoic shales (e.g. Jarvis et al., 1994; Cruse et al., 2000; Shields and Stille 2001; Kidder et al., 2003; Emsbo et al., 2015; Alvaro et al., 2016). It is commonly ascribed to the lithification of apatite concretions in sediments enriched in OM and Fe-oxyhydroxide (e.g. Elderfield et al., 1990; Kidder et al., 2003). The MREE are preferentially adsorbed onto these phases and then transferred to the pore water during their dissolution as redox conditions change (Jarvis et al., 1994; Chen et al., 2015; Alvaro et al., 2016). As apatite frequently formed at the expense of OM in phosphatic and sulphide clasts (Type 2 and Type 3), one can consider a direct uptake of REE from organic matter during its replacement (Fig. 2i and Fig. 3a; see discussion in section 5.1.2). Such direct uptake – without transfer of elements via pore water – would explain why the REE contents are higher in the sulphide clasts compared to the apatite nodules (Fig. 4; see section 4.2). Moreover, MREE uptake could have been favoured by a biogenic influence during phosphate precipitation (Stanley and Byrne 1990; Kidder and Eddy-Dilek 1994), which is plausible considering the microspherulitic texture observed (see section 5.1.2). Finally, it was also suggested that the MREE are preferentially removed from solution when phosphates and REE compounds are co-precipitated (Byrne et al., 1996).

The lack of a significant Ce anomaly in PAAS-normalized REE patterns suggests that the release of Ce and other elements from Fe-oxyhydroxides occurred in anoxic water (e.g. Chen et al., 2015; Alvaro et al., 2016; Gao et al., 2018). These conditions would have prevented Ce^{3+} from being oxidized to insoluble Ce^{4+} , and favoured its adsorption onto oxyhydroxides. The slightly positive Eu/Eu^*_{PAAS} (from 1 to 1.14) precludes extremely reducing conditions (e.g. Kidder et al., 2003) and could indicate contribution from a hydrothermal fluid (Bau et al., 2010; see section 5.3). The low intensity of the Eu anomaly can be explained by the involvement of acidic sulphate-rich hydrothermal brines (Douville et al., 1999; Craddock et al., 2010; Schmidt et al., 2010). Besides, an additional sulphate input to seawater would enhance phosphatisation through increased microbial activity (as shown for the Doushantuo Formation by Cui et al., 2016).

The discussion above addresses the likely processes and environment prevailing at the time of apatite formation, i.e. prior to the reworking of the material from the mineralisation site due to wave or bottom current action (e.g. Pašava et al., 2008). The primary mineralised bed has been interpreted as a subaquatic hardground, formed at moderate depth, close to the oxic – anoxic and sulphide-saturated water interface (e.g. Murowchick et al., 1994; Křibek et al., 2007; Pašava et al., 2008). Such an environment is consistent with the lack of Ce and Eu anomalies observed in apatite, which indicates moderately reducing conditions. Moreover, it would be favourable for bacterial development, which likely played a role in the mineralisation (e.g. Steiner et al., 2001; Křibek et al., 2007). In addition, the hardground was seemingly enriched in Fe and OM (Orberger et al., 2005; Křibek et al., 2007), which are known to act as efficient element scavengers.

The apatite nodules from the Niutitang Formation at Sansha, Longbizui, Jinsha, Songtao and Daotuo are characterised by MREE-enriched PAAS-normalized REE patterns (Zhu et al., 2014; Gao et al., 2018; Ye et al., 2020, 2021). However, at Daotuo, a negative Ce anomaly was noted (from 0.4 to 0.7) and this could reflect an exposure to mildly oxidized water in a transition zone to an intra-platform depression (Zhu et al., 2014; Gao et al., 2018). A positive Eu anomaly (from 1.0 to 2.0) is also observed in the apatite REE patterns from this location. This anomaly varies gradually from one location to another. It is slightly positive at Longbizui, Sancha and Jinsha (average values of ~ 1.1 and 1.2, respectively; Zhu et al., 2014; Ye et al., 2020), moderate at Daotuo (mean value of 1.3; Ye et al., 2021) and more pronounced at Songtao (1.5; Ye et al., 2020). Whatever the intensity of the Eu anomaly, it can be ascribed to the influence of hydrothermal fluids (Zhu et al., 2014; Gao et al., 2018; Ye et al., 2020, 2021).

5.3. Source of elements and hydrothermal influence

In addition to REE patterns and Ce and Eu anomalies, other geochemical parameters (i.e. ΣREE , $\Sigma REE/Th$ and Y/Ho ratios) help to distinguish the origin of apatite-forming elements (dissolved vs terrigenous) and highlight the contribution from other sources (e.g. Chen et al., 2015; Gao et al., 2018; Fig. 6). Authigenic/syndiagenetic Type 2 and Type 3 apatite in the ore bed is characterised by Y/Ho ratios that are intermediate between a hydrogenous and detrital component, suggesting a contribution from both reservoirs. Type 1 apatite plots towards the detrital end-member along a trend line in the Y/Ho vs $\Sigma REE/Th$ diagram (Fig. 6a,b). One can see that authigenic apatite plots off the ideal hydrogenous-terrigenous trend in the Y/Ho vs ΣREE and Y/Ho vs $\Sigma REE/Th$ diagrams (Fig. 6a,b). The REE enrichment compared to the ideal trend suggests a third/external addition of REE to the system, as proposed for other large phosphate deposits in the Niutitang Formation (Gao et al., 2018). This additional input of elements could result (i) from the release of REE scavenged by Fe-oxyhydroxides and their subsequent incorporation into apatite during an early diagenetic phase (as proposed by Gao et al., 2018) or (ii) from the direct uptake when apatite formed at the expense of the OM in phosphatic and sulphide clasts. In the latter case, direct replacement of OM and sulphide by apatite would result in a higher Th content in the phosphate. This explains why the corresponding analyses plot so close to the ideal mixing trend in the Y/Ho vs $\Sigma REE/Th$ diagram (Fig. 6b).

The positive correlation between Ce/Ce^* and the total REE content of apatite (Fig. 6c) can provide more information about the conditions in which apatite formed (for instance, more oxidizing conditions for the detrital apatite and more reducing conditions for the *syn*-sulphide apatite). It could also reveal post-depositional alteration, which typically tends to increase REE contents and reverses Ce depletion (McArthur and Walsh, 1984; Shields and Stille, 2001). However, in the present case and considering the mixing trend in the Y/Ho vs $\Sigma REE/Th$ diagram (Fig. 6b) and in the Y/Ho vs $^{87}Sr/^{86}Sr$ diagram (Fig. 6d, as explained below), the Ce/Ce^* and ΣREE positive correlation support a detrital contribution, which is represented by the Type 1 apatite, and an external

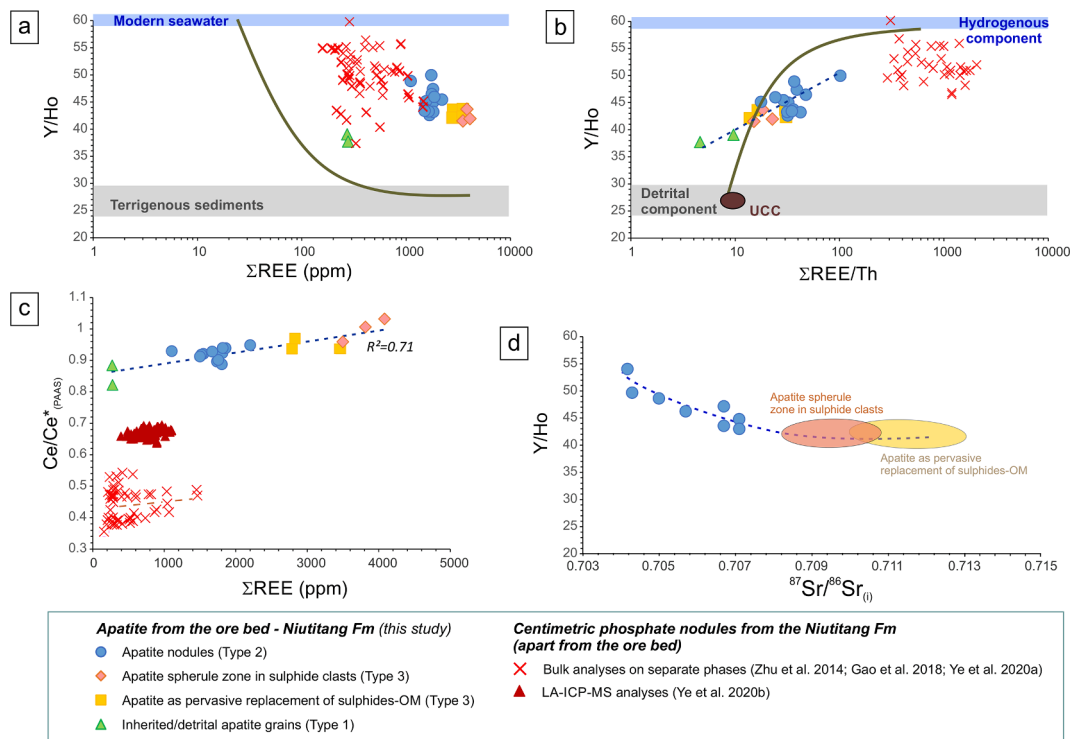


Fig. 6. Correlations for LA-ICP-MS analyses between the Y/Ho ratio and the total REE content (a), the total REE content/Th ratio (b) and the Ce anomaly (PAAS-normalised) and the total REE content (c). Apatite types/generations are referred as (Type 1), (Type 2) and (Type 3) (see text for further explanation). Hydrogenous component/seawater, detrital/inherited component/terrigenous sediments fields and mixing curves are from [Chen et al., \(2015\)](#), the Y/Ho ratio and in-situ $^{87}\text{Sr}/^{86}\text{Sr}_{(t)}$ (d). Fields for “apatite spherule zone in sulphide clasts” and “apatite as pervasive replacement of sulphides-OM” (Type 3 apatite) are drawn to illustrate the variations of the data for these apatite morphotypes, since no perfect match between trace element and isotope data can be properly reported in the (d) figure. Bulk analyses and LA-ICP-MS analyses obtained on other phosphate nodules from the Niutitang Formation are given for comparison.

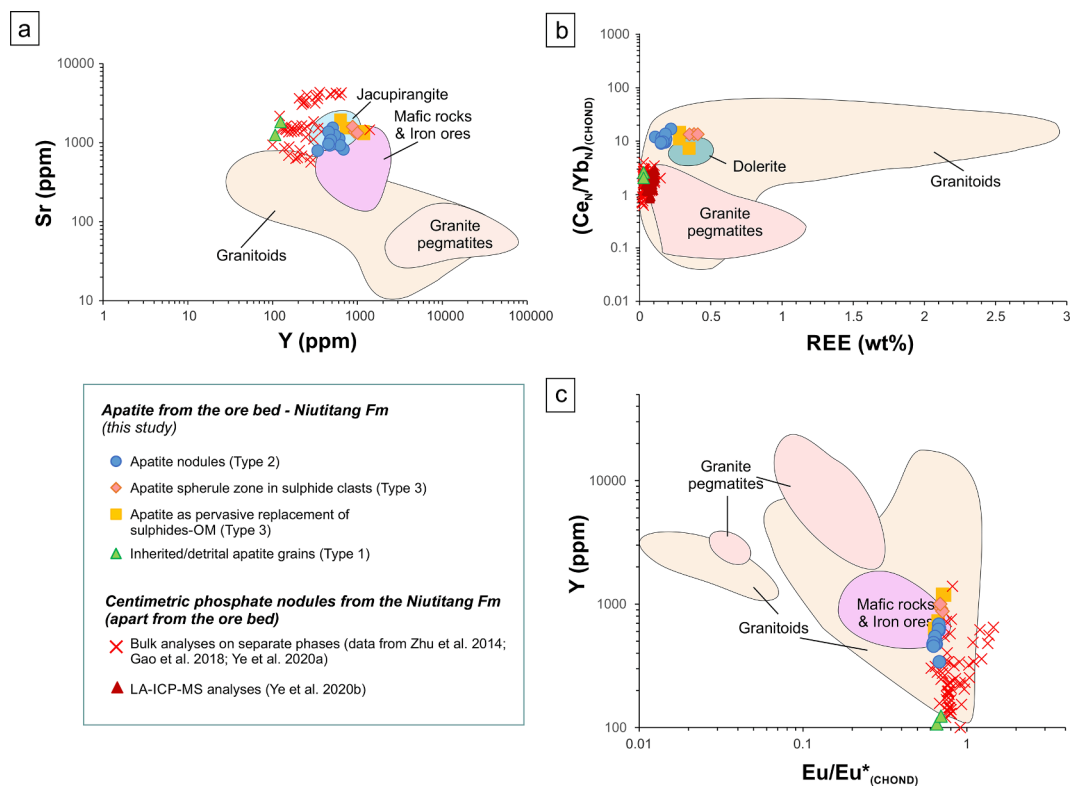


Fig. 7. Discriminant plots for apatite composition and affinity ([Belousova et al., 2002](#)). Correlations for LA-ICP-MS analyses between Sr and Y (a), chondrite-normalised Ce/Yb ratio and total REE content (in %) (b), Y and chondrite-normalised Eu anomaly (c). Apatite types/generations are referred as (Type 1), (Type 2) and (Type 3) (see text for further explanation).

contribution, which could be hydrothermal (as suggested for large phosphate nodules from the Niutitang Formation; Ye et al., 2020). Trace element contents of apatite from the ore bed provide further indirect evidence of the involvement of hydrothermal brines. In the discrimination diagrams of Belousova et al. (2002) (Fig. 7a-c), apatite plots in, or very close to, the mafic rock fields (“mafic rocks and iron ore” in Fig. 7a, c; “dolerite” in Fig. 7b). Such mafic affinity is supported by PGE and Ni enrichment of the sulphides associated with phosphates in the ore bed (Murowchick et al., 1994; Steiner et al., 2001; Pašava et al., 2008, 2019). By comparison, the Type 1 detrital apatite plots rather close to the granitoid fields in these discrimination diagrams, which is consistent with (i) its green CL, which is typical of apatite in granitoids (and associated greisen and pegmatite; e.g. Kempe and Götz 2002; Baele et al., 2019) and (ii) by its slight enrichment in HREE (compared to mafic rocks; Belousova et al., 2002; Fig. 4c,d).

In addition to its trace element signature, the Sr isotope composition of apatite also points at some interaction of a hydrothermal fluid with mafic rocks. Apatite in the ore bed yielded a wide range of initial $^{87}\text{Sr}/^{86}\text{Sr}$ ratios from ~ 0.7000 to 0.7190 . The more radiogenic Sr isotope compositions were observed in zones with a higher density of aluminosilicate/phylosilicate inclusions (Type 1 and Type 2 apatite). Given the small size of the apatite grains, these inclusions could not be avoided during LA-ICP-MS/MS analyses. Sheet silicates have generally a high Rb concentration and will thus lead to elevated $^{87}\text{Sr}/^{86}\text{Sr}$ ratios in comparison to pure apatite. Interestingly, this shift in Sr isotope composition is inversely correlated with spot size (Fig. 5b). One can see that $^{87}\text{Sr}/^{86}\text{Sr}$ ratios are lower but with higher variability when analyses are performed using a small spot size ($20\ \mu\text{m}$), whereas the Sr isotope ratios are higher but more uniform with a larger spot size ($100\ \mu\text{m}$). Laser spots with a diameter of $20\ \mu\text{m}$ were placed in areas dominated by apatite, with fewer aluminosilicate/phylosilicate inclusions. By comparison, laser spots with a diameter of $100\ \mu\text{m}$ are much larger than individual apatite grains. The volume ablated thus represents a mixture of apatite and inclusions. Sr isotope ratios of the latter are consequently higher than the $^{87}\text{Sr}/^{86}\text{Sr}$ ratios from the $20\ \mu\text{m}$ spots. In addition, the zones that are poorer in inclusions, as in several Type 1 apatite nodules, are indeed characterized by the lowest Rb contents. The isotope signature of such apatite would therefore represent the Sr isotope composition closest to the initial ratio. For instance, $^{87}\text{Sr}/^{86}\text{Sr}_i$ in inclusion-free apatite nodules (sample BSC1) is between 0.7032 and 0.7086 . These values are well below 0.709 , which is the average value for Early Cambrian seawater (e.g. Burke et al., 1982; Veizer et al., 1999; Hannisdal and Peters 2011; Fig. 5a). Such low $^{87}\text{Sr}/^{86}\text{Sr}_i$ strongly supports the contribution from hydrothermal fluids with a mafic source, which are characterised by a low $^{87}\text{Sr}/^{86}\text{Sr}$ (0.7030 ; e.g. Von Damm 1990; Jones and Jenkins 2001; Fig. 5a). An external hydrothermal metal contribution is further indicated by the Y/Ho vs $^{87}\text{Sr}/^{86}\text{Sr}_i$ diagram (Fig. 6d). There, a trend highlights the mixing between (i) a reservoir with a higher Y/Ho ratio and the least radiogenic $^{87}\text{Sr}/^{86}\text{Sr}_i$ (corresponding to the external/hydrothermal addition of REE to the system), and (ii) a more detrital pole with low Y/Ho ratios and high Sr isotope compositions. The latter reflects the chemistry of apatite in clasts, which is influenced by phylosilicate inclusions.

In summary, the trace element and Sr isotope signature of apatite supports the contribution of a mafic source to the mineralizing system through hydrothermal processes. This scenario is in agreement with the model proposed for the origin of Ni (and PGE) in the mineralised bed (e.g. Steiner et al., 2001; Pašava et al., 2008), which is based – among others – on the light $\delta^{60}\text{Ni}$ signature of sulphides (Pašava et al., 2019), well comparable with that of sulphides hosted by Archean komatiites from Australia and Canada (Gueguen et al., 2013) or Zimbabwe (Hofmann et al., 2014). This isotopic signature suggests an external metal source, which could have been hydrothermal alteration of mafic/ultramafic rocks (Pašava et al., 2019). The metamorphic basement of the Yangtze Platform consists of a poorly exposed Archean nucleus (Zheng et al., 2006) overlain by Paleo- to Early Neoproterozoic, slightly

metamorphic igneous and sedimentary rocks, including rift- or plume-related komatiitic basalt and ultramafic intrusions (Huang and Wang 2019; Mao and Du 2002; Wang et al., 2007; Zhou et al., 2017). Rifts in combination with basinal brines can have a variety of sub-seafloor fluid systems such as cold seeps and low temperature hydrothermal vents, which may tap and leach unexposed mafic-ultramafic rocks in the basement (Lehmann et al., 2022). In the Yangtze Craton, these mafic-ultramafic magmatic rocks of Neoproterozoic age indeed host occurrences of Fe-Ni-Cu sulphides (as at Baotan, Fig. 1a; Mao and Du 2002; Zhou et al., 2017) and locally contain high PGE concentrations (which are well documented at Fanjingshan, Fig. 1a; Huang and Wang 2019). In addition, intense hydrothermal venting at the time is documented along the margin of the Yangtze Craton by numerous contemporaneous SEDEX-type (barite) deposits (e.g. Emsbo et al., 2005; Han et al., 2020; Pašava et al., 2008; Pi et al., 2014; Xia et al., 2004; Fig. 1a).

As proposed by Murowchick et al. (1994), it seems as if metals had been introduced repeatedly into the depositional basin by hydrothermal brines. This applies specifically to metals of mafic affinity that are concentrated in apatite, namely the REE, Y and Sr. According to the same authors, apatite would have formed during times of hydrothermal quiescence. Consequently, REE (as Y and Sr) must have been scavenged as soon as they arrived in the mineralising system (during times of hydrothermal input, with no phosphatisation), and were incorporated in the structure of apatite later on, when phosphatisation took place (Fig. 8). This could have been easily achieved through adsorption of these elements onto Fe-oxyhydroxides and/or OM (as discussed under section 5.2). Such a metal addition to the system corresponds to the external component mentioned above (Fig. 6).

In contrast to the metals sourced from hydrothermal brines, other elements originated solely from seawater, either via direct uptake or through scavenging by OM, Fe-Mn oxyhydroxides and/or aluminosilicates. This has been confirmed for Mo and Hg, based on isotopic studies (Mao et al., 2002; Lehmann et al., 2003; Xu et al., 2013; Yin et al., 2017). This would also be the case for phosphorus, which constitutes a major component of the mineralised system, because hydrothermal brines typically contain less P than (bottom) seawater (e.g. Wheat et al., 1996). Instead, detrital OM, Fe-oxyhydroxides and sheet silicates would have provided phosphate to the pore water during local changes in the redox conditions in microenvironments and associated microbial activity (e.g. Jarvis et al., 1994; Krajewski et al., 1994; Föllmi 1996; Filippelli 2011).

6. Conclusions

This study focused on the petrological, mineralogical, geochemical and in-situ Sr isotope analyses of apatite from the ore bed in the Niutitang Formation (Huangjiawan mine, Zunyi region, Southern China). In the ore bed, apatite shows variable types. A very rare detrital apatite - Type 1 apatite - is present as green luminescing grains in the dolomitic shale. Two types of authigenic carbonate-fluorapatite exhibiting a REE-activated, (dull)-violet CL can be distinguished in the ore bed. Type 2 apatite occurs as nodules of aggregates of micrometric euhedral crystals and as microspherules replacing organic matter in phosphatic clasts. Type 3 apatite is found in sulphide clasts (i) as microspherules that replaced pyrite, a Mo-C-S phase and organic matter and (ii) as pervasive replacement (of the same sulphides and Mo-C-S phase) following an irregular pattern (and without any extent outside of the clast).

Regarding the textures and their meaning, the spherulitic microtextures in phosphatic and sulphide clasts (Types 2 and 3) are reminiscent of microbially-mediated precipitates. The nature of the inclusions found in apatite nodules (Type 2) and their sub-angular (to sub-rounded) shape testify of (short distance) transport. The same holds true for phosphatic and sulphide clasts (Types 2 and 3). Textural evidence confirms that both phosphate and sulphide mineralisation were roughly coeval and occurred prior to reworking of the clasts into deeper marine environments.

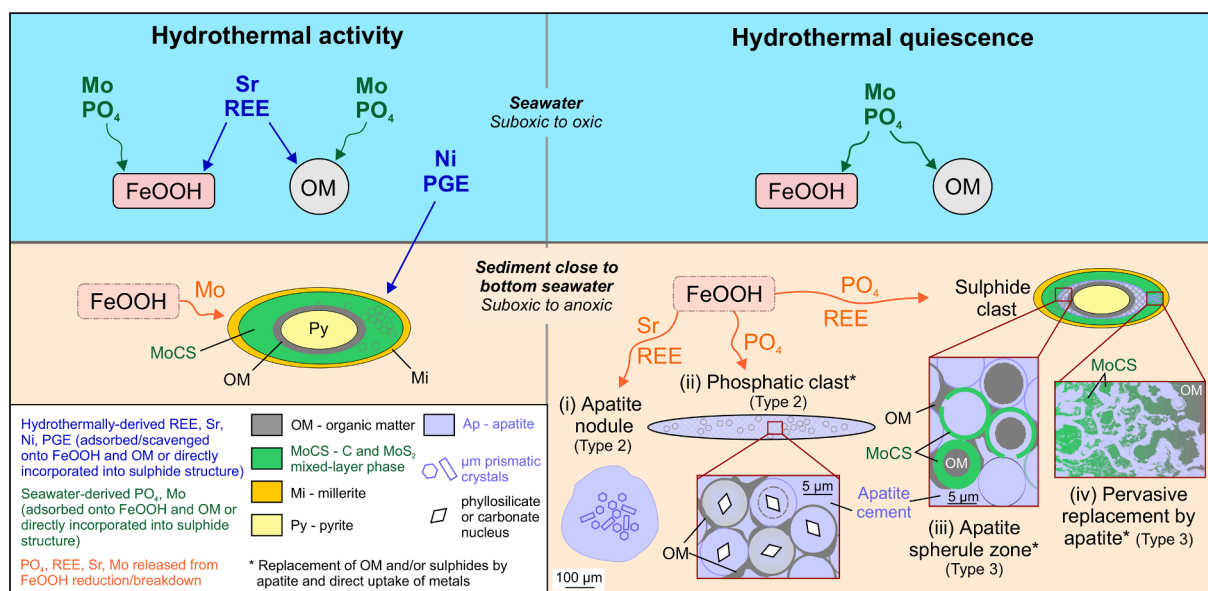


Fig. 8. Simplified model for the formation of apatite and origin of elements in the ore bed of the Niutitang Formation. During periods of hydrothermal activity, REE and Sr from hydrothermal brines are adsorbed onto Fe oxyhydroxide (FeOOH) and OM, while Ni and PGE enter sulphide structure. Mo is released from FeOOH (which is reduced and destabilised) or recycled from the OM that is replaced by sulphides. During periods of hydrothermal quiescence, PO_4 , REE and Sr – which were previously adsorbed onto FeOOH – are released when Fe oxyhydroxide is reduced. Subsequent saturation in phosphate of the porewater at the bottom seawater-sediment interface results in the formation of apatite, which also incorporates REE and Sr. Apatite forms: (i) nodules made of micrometric prismatic crystals; (ii) spherules replacing OM around a carbonate/silicate nucleus in phosphatic clasts; (iii) spherules replacing Mo—C—S ooids and OM in sulphide clasts. The intensity of replacement is variable from one spherule to another. In phosphatic and sulphide clasts, apatite cement fills the remaining porosity around the spherules in association with OM. Spherule habits would testify for microbially-mediated phosphogenesis. In sulphide clasts, apatite also replaces Mo—C—S and OM in more pervasive way (iv).

Concerning their trace element contents, all authigenic apatite morphotypes share common characteristics that are (i) an enrichment in MREE, which highlights the main role played by Fe-oxyhydroxides and OM in scavenging trace elements, and (ii) the lack of Ce and Eu anomalies, which indicates slightly reducing conditions. The trace element signatures of Types 2 and 3 apatite (REE, Y and Sr) point to significant contribution of a mafic source to the mineralization processes during phosphogenesis. Consistently, the lowest initial Sr isotope compositions obtained in-situ on Type 2 apatite (LA-ICP-MS data) further confirm such a contribution from hydrothermal fluids that have interacted with mafic rocks, whereas more radiogenic Sr isotopic ratios, which are higher than average for Lower Cambrian seawater, resulted in all likelihood from contamination by phyllosilicate inclusions. However, other elements - like P - are unlikely to originate from hydrothermal fluids but were instead derived entirely from seawater through scavenging onto Fe-oxyhydroxides and OM, and subsequent release.

The data obtained provide new information about phosphogenesis and polymetallic sulphide mineralisation. A simplified model for the formation of apatite and origin of elements can be summarised as follows: During periods of hydrothermal activity, REE and Sr from hydrothermal brines were adsorbed onto Fe-oxyhydroxide and OM, while Ni and PGE entered sulphides. Mo was released from the breakdown of Fe-oxyhydroxide or recycled from the OM that became replaced by sulphides. In contrast, during periods of hydrothermal quiescence, phosphate, REE and Sr were released when Fe-oxyhydroxide were reduced. Subsequent supersaturation in phosphate of the porewater at the bottom seawater-sediment interface resulted in the formation of apatite, which also incorporated REE and Sr.

The contribution of hydrothermal fluids and the magmatic origin of several metals – as highlighted by this study – constitute a key finding that opens new research directions on the metals' ultimate source, which is important for any future exploration strategy for this type of ore.

Declaration of Competing Interest

The authors declare that they have no known competing financial interests or personal relationships that could have appeared to influence the work reported in this paper.

Data availability

No data was used for the research described in the article.

Acknowledgments

The authors would like to express their gratitude to Ulrich Schüssler and Stefan Höhn for their assistance in acquiring electron microprobe analyses at the University of Würzburg. Chantal Peiffert is warmly thanked for help in acquiring LA-ICP-MS analyses. The authors thank Thomas Goovaerts for helping to improve the English of the manuscript. The research was partly funded by the Belgian Federal Science Policy Office (BELSPO) - BRAIN program (DESIRED projects). The LA-ICP-MS laboratory from GeoRessources was partly funded by the French National Research Agency through the national program "Investissements d'avenir" of the Labex Ressources21 with the reference ANR-10-LABX-21-RESSOURCES21. This is also a contribution to the Strategic Research Plan of the Czech Geological Survey (DKRVO 2018-2022). The authors also warmly thank Franco Pirajno (Editor), and two anonymous reviewers, for helpful remarks on the manuscript. Their comments have contributed to improve substantially the quality of this paper.

Appendix A. Supplementary data

Supplementary data to this article can be found online at <https://doi.org/10.1016/j.oregeorev.2022.105130>.

References

- Álvarez, J.J., Shields-Zhou, G.A., Ahlberg, P., Jensen, S., Palacios, T., Fairchild, I., 2016. Ediacaran-Cambrian phosphorites from the western margins of Gondwana and Baltica. *Sedimentology* 63 (2), 350–377.
- Baele, J.M., Decrée, S., Rusk, B., 2019. Cathodoluminescence applied to ore geology and exploration. In: Decrée, S., Robb, L. (Eds.), *Ore Deposits: Origin, Exploration, and Exploitation*. Wiley, New York, pp. 131–161.
- Bau, M., Balan, S., Schmidt, K., Koschinsky, A., 2010. Rare earth elements in mussel shells of the Mytilidae family as tracers for hidden and fossil high-temperature hydrothermal systems. *Earth Planet. Sci. Lett.* 299 (3–4), 310–316.
- Belousova, E.A., Griffin, W.L., O'Reilly, S.Y., Fisher, N.L., 2002. Apatite as an indicator mineral for mineral exploration: trace-element compositions and their relationship to host rock type. *J. Geochem. Explor.* 76 (1), 45–69.
- Blanc, P., Baumer, A., Cesbron, F., Ohnenstetter, D., Panczer, G., Rémond, G., 2000. In: *Cathodoluminescence in Geosciences*. Springer Berlin Heidelberg, Berlin, Heidelberg, pp. 127–160.
- Bouzari, F., Hart, C.J.R., Bissig, T., Barker, S., 2016. Hydrothermal alteration revealed by apatite luminescence and chemistry: a potential indicator mineral for exploring covered porphyry copper deposits. *Econ. Geol.* 111 (6), 1397–1410.
- Bruand, E., Storey, C., Fowler, M., 2016. An apatite for progress: Inclusions in zircon and titanite constrain petrogenesis and provenance. *Geology* 44 (2), 91–94.
- Burke, W.H., Denison, R.E., Hetherington, E.A., Koepnick, R.B., Nelson, H.F., Otto, J.B., 1982. Variation of seawater $87\text{Sr}/86\text{Sr}$ throughout Phanerozoic time. *Geology* 10, 516–519.
- Byrne, R.H., Liu, X., Schijf, J., 1996. The influence of phosphate coprecipitation on rare earth distributions in natural waters. *Geochim. Cosmochim. Acta* 60 (17), 3341–3346.
- Chen, J., Algeo, T.J., Zhao, L., Chen, Z.Q., Cao, L., Zhang, L., Li, Y., 2015. Diagenetic uptake of rare earth elements by bioapatite, with an example from Lower Triassic conodonts of South China. *Earth Sci. Res.* 149, 181–202.
- Chen, Y., Jiang, S., Ling, H., Feng, H., Yang, J., Chen, J., 2003. Pb-Pb isotope dating of black shales from the lower Cambrian Niutitang formation, Guizhou Province, South China. *Prog. Nat. Sci.* 13 (10), 771–776.
- Chen, Q., Sun, M., Long, X., Zhao, G., Wang, J., Yu, Y., Yuan, C., 2018. Provenance study for the Paleozoic sedimentary rocks from the west Yangtze Block: constraint on possible link of South China to the Gondwana supercontinent reconstruction. *Precamb. Res.* 309, 271–289.
- Chen, D., Wang, J., Qing, H., Yan, D., Li, R., 2009. Hydrothermal venting activities in the Early Cambrian, South China: petrological, geochronological and stable isotopic constraints. *Chem. Geol.* 258 (3–4), 168–181.
- Chen, N.C., Yang, X., Liu, D., Xiao, X., Fan, D.L., Wang, L., 1982. Lower Cambrian black argillaceous and arenaceous rock series in south China and its associated stratiform deposits. *Miner. Deposita* 1, 39–51.
- Choquette, P.W., Hiatt, E.E., 2008. Shallow-burial dolomite cement: a major component of many ancient sucrosic dolomites. *Sedimentology* 55 (2), 423–460.
- Condie, K.C., 1993. Chemical composition and evolution of the upper continental crust: contrasting results from surface samples and shales. *Chem. Geol.* 104 (1–4), 1–37.
- Coveney, R.M., Nansheng, C., 1991. Ni-Mo-PGE-Au-rich ores in Chinese black shales and speculations on possible analogues in the United States. *Miner. Deposita* 26 (2), 83–88.
- Craddock, P.R., Bach, W., Seewald, J.S., Rouxel, O.J., Reeves, E., Tivey, M.K., 2010. Rare earth element abundances in hydrothermal fluids from the Manus Basin, Papua New Guinea: Indicators of sub-seafloor hydrothermal processes in back-arc basins. *Geochim. Cosmochim. Acta* 74 (19), 5494–5513.
- Cruse, A.M., Lyons, T.W., & Kidder, D.L. (2000). Rare-earth element behavior in phosphates and organic-rich host shales: an example from the Upper Carboniferous of Midcontinent North America.
- Cui, H., Xiao, S., Zhou, C., Peng, Y., Kaufman, A.J., Plummer, R.E., 2016. Phosphogenesis associated with the Shuram Excursion: petrographic and geochemical observations from the Ediacaran Doushantuo Formation of South China. *Sed. Geol.* 341, 134–146.
- Decrée, S., Cawthorn, G., Deloué, E., Mercadier, J., Frimmel, H., Baele, J.M., 2020. Unravelling the processes controlling apatite formation in the Phalaborwa Complex (South Africa) based on combined cathodoluminescence, LA-ICP-MS and in-situ O and Sr isotope analyses. *Contrib. Miner. Petrol.* 175, 1–31.
- Douville, E., Bienvenu, P., Charlou, J.L., Donval, J.P., Fouquet, Y., Appriou, P., Gamo, T., 1999. Yttrium and rare earth elements in fluids from various deep-sea hydrothermal systems. *Geochim. Cosmochim. Acta* 63 (5), 627–643.
- Elburg, M., Vroon, P., van der Wagt, B., Tchalikian, A., 2005. Sr and Pb isotopic composition of five USGS glasses (BHVO-2G, BIR-1G, BCR-2G, TB-1G, NKT-1G). *Chem. Geol.* 223 (4), 196–207.
- Elderfield, H., Upstill-Goddard, R., Sholkovitz, E.R., 1990. The rare earth elements in rivers, estuaries, and coastal seas and their significance to the composition of ocean waters. *Geochim. Cosmochim. Acta* 54 (4), 971–991.
- Emo, R.B., Smit, M.A., Schmitt, M., Kooijman, E., Scherer, E.E., Sprung, P., Bleeker, W., Mezger, K., 2018. Evidence for evolved Hadean crust from Sr isotopes in apatite within Eoarchean zircon from the Acasta Gneiss Complex. *Geochimica et Cosmochim. Acta* 235, 450–462.
- Emsbo, P., Hofstra, A.H., Johnson, C.A., Koenig, A., Grauch, R., Zhang, X.C., et al., (2005). Lower Cambrian metallogenesis of south China: interplay between diverse basinal hydrothermal fluids and marine chemistry. In *Mineral deposit research: Meeting the global challenge* (pp. 115–118). Springer, Berlin, Heidelberg.
- Emsbo, P., McLaughlin, P.I., Breit, G.N., du Bray, E.A., Koenig, A.E., 2015. Rare earth elements in sedimentary phosphate deposits: Solution to the global REE crisis? *Gondwana Res.* 27 (2), 776–785.
- Fan, D., 1983. Polyelements in the Lower Cambrian black shale series in southern China. In: Augistithis, S.S. (Ed.), *The Significance of Trace Metals in Solving Petrogenetic Problems and Controversies*. Theophrastus Publications S.A, Athens, pp. 447–474.
- Filippelli, G.M., 2011. Phosphate rock formation and marine phosphorus geochemistry: the deep time perspective. *Chemosphere* 84 (6), 759–766.
- Follmi, K., 1996. The phosphorus cycle, phosphogenesis and marine phosphate-rich deposits. *Earth Sci. Rev.* 40 (1–2), 55–124.
- Frimmel, H.E., & Spangenberg, J.E. (2007). Molecular and compound-specific isotopic composition of hydrocarbons in Lower Cambrian black shales from the Yangtze Platform, South China. Andrew, C. et al., (eds.), *Digging Deeper*, Proc. 9th Biennial SGA Meeting, 20-23 August 2007, Irish Assoc. Econ. Geol., Dublin, v. 1, p. 801-804.
- Fu, Y., Dong, L., Li, C., Qu, W., Pei, H., Qiao, W., Shen, B., 2016. New Re-Os isotopic constrains on the formation of the metalliferous deposits of the Lower Cambrian Niutitang formation. *J. Earth Sci.* 27 (2), 271–281.
- Gao, P., He, Z., Li, S., Lash, G.G., Li, B., Huang, B., Yan, D., 2018. Volcanic and hydrothermal activities recorded in phosphate nodules from the Lower Cambrian Niutitang Formation black shales in South China. *Palaeogeogr. Palaeoclimatol. Palaeoecol.* 505, 381–397.
- Gillespie, J., Nemchin, A.A., Kinny, P.D., Martin, L., Aleshin, M., Roberts, M.P., et al., 2020. Strontium isotope analysis of apatite via SIMS. *Chem. Geol.* 559, 119979.
- Goldoff, B., Webster, J.D., Harlow, D.E., 2012. Characterisation of fluor-chlorapatites by electron probe microanalysis with a focus on time-dependent intensity variation of halogens. *Am. Mineral.* 97, 1103–1115.
- Gueguen, B., Rouxel, O., Ponzevera, E., Bekker, A., Fouquet, Y., 2013. Nickel isotope variations in terrestrial silicate rocks and geological reference materials measured by MC-ICP-MS. *Geostand. Geoanal. Res.* 37 (3), 297–317.
- Han, T., Zhu, X.Q., Li, K., Jiang, L., Zhao, C.H., Wang, Z.G., 2015. Metal sources for the polymetallic Ni-Mo-PGE mineralization in the black shales of the Lower Cambrian Niutitang Formation, South China. *Ore Geol. Rev.* 67, 158–169.
- Han, T., Fan, H., Zhu, X., Wen, H., Zhao, C., Xiao, F., 2017. Submarine hydrothermal contribution for the extreme element accumulation during the early Cambrian, South China. *Ore Geol. Rev.* 86, 297–308.
- Han, T., Fan, HaiFeng, Wen, HanJie, Mo, B., Murowchick, J.B., Lu, ZhiTong, Algeo, T.J., 2020. Petrography and sulfur isotopic compositions of SEDEX ores in the early Cambrian Nanhua Basin, South China. *Precamb. Res.* 345, 105757.
- Hannisdal, B., Peters, S.E., 2011. Phanerozoic Earth system evolution and marine biodiversity. *Science* 334 (6059), 1121–1124.
- Hiatt, E.E. & Pufahl, P.K. (2014). Cathodoluminescence petrography of carbonate rocks: application to understanding diagenesis, reservoir quality, and pore system evolution: in Coulson, I. (ed.) *Cathodoluminescence and Its Application to Geoscience: Mineralogical Association of Canada, Short Course Series Volume 45*, p. 75–96.
- Hiatt, E.E., & Pufahl, P.K., (2014). Cathodoluminescence petrography of carbonate rocks: application to understanding diagenesis, reservoir quality, and pore system evolution: in Coulson, I. (ed.) *Cathodoluminescence and Its Application to Geoscience: Mineralogical Association of Canada, Short Course Series Volume 45*, p. 75–96.
- Hofmann, A., Bekker, A., Dirks, P., Gueguen, B., 2014. Comparing orthomagmatic and hydrothermal mineralization models for komatiite-hosted nickel deposits in Zimbabwe using multiple sulfur, iron, and nickel isotope data. *Miner. Deposita* 49, 75–100.
- Hogmalm, K.J., Zack, T., Karlsson, A.-O., Sjöqvist, A.S.L., Garbe-Schönberg, D., 2017. In situ Rb-Sr and K-Ca dating by LA-ICP-MS/MS: an evaluation of N 2 O and SF 6 as reaction gases. *J. Anal. At. Spectrom.* 32 (2), 305–313.
- Huang, S., Wang, W., 2019. Origin of the Fanjingshan mafic-ultramafic rocks, Western Jiangnan Orogen, South China: Implications for PGE fractionation and mineralisation. *J. Earth Sci.* 30, 258–271.
- Jacquemin, D. (2020). The phosphatic chalk of the Mons Basin, Belgium. Petrography and geochemistry of the Ciplé Phosphatic Chalk and implications on its genesis. *Memoirs of the Geological Survey of Belgium Vol. 64*, 93 pages (in press).
- Jarvis, I., Burnett, W., Baturin, G.N., 1994. Geochemistry of phosphorite-state of the art. *Ecolage Geol. Helv.* 87, 643–671.
- Jia, Z., Hou, D., Sun, D., Jiang, Y., Zhang, Z., Hong, M., 2018. Geochemical characteristics of source rocks in the Lower Cambrian Niutitang Formation in Guizhou Province, China. *J. Nat. Gas Geosci.* 3 (5), 263–272.
- Jiang, S.-Y., Chen, Y.-Q., Ling, H.-F., Yang, J.-H., Feng, H.-Z., Ni, P., 2006. Trace-and rare-earth element geochemistry and Pb-Pb dating of black shales and intercalated Ni-Mo-PGE-Au sulfide ores in Lower Cambrian strata, Yangtze Platform, South China. *Miner. Deposita* 41 (5), 453–467.
- Jiang, S., Yang, J., Ling, H., Feng, H., Chen, Y., Chen, J., 2003. Re-Os isotopes and PGE geochemistry of black shales and intercalated Ni-Mo polymetallic sulfide bed from the Lower Cambrian Niutitang Formation, South China. *Prog. Nat. Sci.* 13 (10), 788–794.
- Jiang, S.-Y., Yang, J.-H., Ling, H.-F., Chen, Y.-Q., Feng, H.-Z., Zhao, K.-D., Ni, P., 2007. Extreme enrichment of polymetallic Ni-Mo-PGE-Au in Lower Cambrian black shales of South China: an Os isotope and PGE geochemical investigation. *Palaeogeogr. Palaeoclimatol. Palaeoecol.* 254 (1–2), 217–228.
- Jiang, S.-Y., Pi, D.-H., Heubeck, C., Frimmel, H.E., Liu, Y.-P., Deng, H.-L., Ling, H.-F., Yang, J.-H., Zhu, M., 2009. Early Cambrian ocean anoxia in South China. *Nature* 459, E5–E6.
- Jochum, K.P., Weis, U., Stoll, B., Kuzmin, D., Yang, Q., Raczek, I., Jacob, D.E., Stracke, A., Birbaum, K., Frick, D.A., Günther, D., Enzweiler, J., 2011. Determination of reference values for NIST SRM 610–617 glasses following ISO guidelines. *Geostand. Geoanal. Res.* 35 (4), 397–429.

- Jones, C.E., Jenkyns, H.C., 2001. Seawater strontium isotopes, oceanic anoxic events, and seafloor hydrothermal activity in the Jurassic and Cretaceous. *Am. J. Sci.* 301, 112–149.
- Kao, L.S., Peacor, D.R., Coveney Jr., R.M., Zhao, G., Dungey, K.E., Curtis, M.D., Penner-Hahn, J.E., 2001. A C/MoS₂ mixed-layer phase (MoCS) occurring in metalliferous black shales from southern China, and new data on jordisite. *Am. Mineral.* 86, 852–861.
- Kempe, U., Götze, J., 2002. Cathodoluminescence (CL) behaviour and crystal chemistry of apatite from rare-metal deposits. *Mineral. Mag.* 66, 151–172.
- Kidder, D.L., Eddy-Dilek, C.A., 1994. Rare-earth element variation in phosphate nodules from midcontinent Pennsylvanian cyclothem. *J. Sediment. Res.* 64, 584–592.
- Kidder, D.L., Krishnaswamy, R., Mapes, R.H., 2003. Elemental mobility in phosphatic shales during concretion growth and implications for provenance analysis. *Chem. Geol.* 198 (3–4), 335–353.
- Krajewski, K.P., Cappellen, P.V., Trichet, J., Kuhn, O., Lucas, J., Martín-Algarra, A., et al., 1994. Biological processes and apatite formation in sedimentary environments. *Eclogae Geol. Helv.* 87, 701–746.
- Křibek, B., Šýkorová, I., Pašava, J., Machovič, V., 2007. Organic geochemistry and petrology of barren and Mo–Ni–PGE mineralised marine black shales of the Lower Cambrian Niutitang Formation (South China). *Int. J. Coal Geol.* 7, 240–256.
- Lehmann, B., Mao, J., Li, S., Zhang, G., Zeng, M., 2003. Re–Os dating of polymetallic Ni–Mo–PGE–Au mineralisation in Lower Cambrian black shales of South China and its geological significance—A REPLY. *Econ. Geol.* 9, 663–665.
- Lehmann, B., Nägler, T.F., Holland, H.D., Wille, M., Mao, J., Pan, J., Ma, D., Dulski, P., 2007. Highly metalliferous carbonaceous shale and Early Cambrian seawater. *Geology* 35 (5), 403.
- Lehmann, B., Frei, R., Xu, L., Mao, J., 2016. Early Cambrian black shale-hosted Mo–Ni and V mineralisation on the rifted margin of the Yangtze Platform, China: reconnaissance chromium isotope data and a refined metallogenic model. *Econ. Geol.* 111, 89–103.
- Lehmann, B., Pašava, J., Šebek, O., Andronikov, A., Frei, R., Xu, L., Mao, J., 2022. Early Cambrian highly metalliferous black shale in South China: Cu and Zn isotopes and a short review of other non-traditional stable isotopes. *Miner. Deposita* 57 (7), 1167–1187.
- Li, Z., Duan, D., Jiang, S., Ma, Y., Yuan, H., 2018. In-situ analysis of major elements, trace elements and Sr isotopic compositions of apatite from the granite in the Chengchao skarn-type Fe deposit, Edong ore district: Implications for petrogenesis and mineralisation. *Journal of Earth Sciences* 29, 295–306.
- Li, X., Han, T., Zhu, X., Li, Y., Zheng, Y., Shen, H., 2013. A mineralogical application of micro-PIXE technique: The Ni–Mo–PGE polymetallic layer of black shales in Zunyi region, South China. *Nuclear Instruments & Methods in Physics Research Section B-Beam Interactions With Materials And Atoms* 308, 1–5.
- Ling, H., Jiang, S., Feng, H., Chen, Y., Chen, J., Yang, J., 2004. Oxygen isotope geochemistry of phosphorite and dolomite and palaeo-ocean temperature estimation: a case study from the Neoproterozoic Doushantuo Formation, Guizhou Province, South China. *Progress in Natural Science* 14 (1), 77–84.
- Longerich, H.P., Jackson, S.E., Günther, D., 1996. Inter-laboratory note. Laser ablation inductively coupled plasma mass spectrometric transient signal data acquisition and analyte concentration calculation. *J. Anal. At. Spectrom.* 11, 899–904.
- Lott, D.A., Coveney, R.M., Murowichick, J.B., Grauch, R.L., 1999. Sedimentary exhalative nickel-molybdenum ores in South China. *Econ. Geol.* 94, 1051–1066.
- Mao, J., Du, A., 2002. The 982 Ma Re–Os age of copper-nickel sulphide ores in the Baotan area, Guangxi and its geological significance. *Sci. China, Ser. D Earth Sci.* 45, 911–920.
- Mao, J., Lehmann, B., Du, A., Zhang, G., Ma, D., Wang, Y., et al., 2002. Re–Os dating of polymetallic Ni–Mo–PGE–Au mineralisation in Lower Cambrian black shales of South China and its geologic significance. *Econ. Geol.* 97, 1051–1061.
- Marshall, D.J., 1988. Cathodoluminescence of Geological Materials. Hyman, Boston, p. 146.
- Mcarthur, J.M., 1985. Francolite geochemistry—compositional controls during formation, diagenesis, metamorphism and weathering. *Geochim. Cosmochim. Acta* 49 (1), 23–35.
- McArthur, J.M., Walsh, J.N., 1984. Rare-earth geochemistry of phosphorites. *Chem. Geol.* 47 (3–4), 191–220.
- McCLELLAN, G.H., Van kauenbergh, S.J., 1991. Mineralogical and chemical variation of francolites with geological time. *Journal of the Geological Society* 148 (5), 809–812.
- McDonough, W.F., Sun, S.-s., 1995. The composition of the Earth. *Chem. Geol.* 120 (3–4), 223–253.
- Mitchell, R.H., Xiong, J., Mariano, A.N., Fleet, M.E., 1997. Rare-earth-element-activated cathodoluminescence in apatite. *The Canadian Mineralogist* 35, 979–998.
- Mitchell, R.H., Wahl, R., Cohen, A., 2020. Mineralogy and genesis of pyrochlore apatite from The Good Hope Carbonate, Ontario: A potential niobium deposit. *Mineral. Mag.* 84 (1), 81–91.
- Mitchell, R.H. (2014). Cathodoluminescence of apatite. *Mineralogical Association of Canada Short Course 45, Fredericton NB, May 2014, 143–167.*
- Murowichick, J.B., Coveney, R.M., Grauch, R.L., Eldridge, C.S., Shelton, K.L., 1994. Cyclic variations of sulfur isotopes in Cambrian stratatound Ni–Mo–(PGE–Au) ores of southern China. *Geochim. Cosmochim. Acta* 58 (7), 1813–1823.
- Orberger, B., Wagner, C., Vymazalova, A., Pašava, J., Křibek, B., & Gallien, J. P. (2005). Rare metal sequestration and mobility in mineralised black shales from the Zunyi region, South China. In *Mineral Deposit Research: Meeting the Global Challenge*, Mao, J., Bierlein, F.P. (Eds.) Proceedings of the Eighth Biennial SGA Meeting, Beijing, China, 18–21 August 2005, Springer, Berlin, Heidelberg, 167–170.
- Orberger, B., Vymazalova, A., Wagner, C., Fialin, M., Gallien, J.P., Wirth, R., Pašava, J., Montagnac, G., 2007. Biogenic origin of intergrown Mo-sulphide and carbonaceous matter in Lower Cambrian black shales (Zunyi Formation, southern China). *Chem. Geol.* 238 (3–4), 213–231.
- Pağs, A., Barnes, S., Schmid, S., Coveney, R.M., Schwark, L., Liu, W., Grice, K., Fan, H., Wen, H., 2018. Geochemical investigation of the lower Cambrian mineralised black shales of South China and the late Devonian Nick deposit, Canada. *Ore Geol. Rev.* 94, 396–413.
- Pasava, J., Frimmel, H., Taiyi, L., Koubova, M., Martinek, K., 2010. Extreme PGE concentrations in Lower Cambrian acid tuff layer from the Kunyang phosphate deposit, Yunnan province, South China—possible PGE source for Lower Cambrian Mo–Ni–polyelement ore beds. *Econ. Geol.* 105 (6), 1047–1056.
- Pašava, J., Křibek, B., Vymazalová, A., Šýkorová, I., Žák, K., Orberger, B., 2008. Multiple sources of metals of mineralisation in Lower Cambrian black shales of South China: Evidence from geochemical and petrographic study. *Resour. Geol.* 58, 25–42.
- Pašava, J., Zaccarini, F., Aiglsperger, T., Vymazalova, A., 2013. Platinum-group elements (PGE) and their principal carriers in metal-rich black shales: an overview with a new data from Mo–Ni–PGE black shales (Zunyi region, Guizhou Province, south China). *J. Geosci.* 58, 213–220.
- Pašava, J., Ackerman, L., Halodová, P., Pour, O., Đurišová, J., Zaccarini, F., Aiglsperger, T., Vymazalová, A., 2017. Concentrations of platinum-group elements (PGE), Re and Au in arsenian pyrite and millerite from Mo–Ni–PGE–Au black shales (Zunyi region, Guizhou Province, China): results from LA-ICP-MS study. *Eur. J. Mineral.* 29 (4), 623–633.
- Pašava, J., Chrastný, V., Loukola-Ruskeeniemi, K., Šebek, O., 2019. Nickel isotopic variation in black shales from Bohemia, China, Canada, and Finland: a reconnaissance study. *Miner. Deposita* 54 (5), 719–742.
- Paton, C., Hellstrom, J., Paul, B., Woodhead, J., Hergt, J., 2011. Iolite: Freeware for the visualisation and processing of mass spectrometric data. *J. Anal. At. Spectrom.* 26, 2508–2518.
- Penel, G., Leroy, G., Rey, C., Bres, E., 1998. MicroRaman Spectral Study of the PO₄ and CO₃ vibrational modes in synthetic and biological apatites. *Calcif. Tissue Int.* 63 (6), 475–481.
- Pi, D.H., Liu, C.Q., Shields-Zhou, G.A., Jiang, S.Y., 2013. Trace and rare earth element geochemistry of black shale and kerogen in the early Cambrian Niutitang Formation in Guizhou province, South China: Constraints for redox environments and origin of metal enrichments. *Precamb. Res.* 225, 218–229.
- Pi, D.H., Jiang, S.Y., Luo, L., Yang, J.H., Ling, H.F., 2014. Depositional environments for stratiform walterite deposits in the Lower Cambrian black shale sequence of the Yangtze Platform, southern Qinling region, SW China: Evidence from redox-sensitive trace element geochemistry. *Palaeogeogr. Palaeoclimatol. Palaeoecol.* 398, 125–131.
- Potts, P.J., Tindle, A.G., 1989. Analytical characteristics of a multilayer dispersion element (2d=60Å) in the determination of fluorine in minerals by electron microprobe. *Mineral. Mag.* 53 (371), 357–362.
- Ravindran, A., Mezger, K., Balakrishnan, S., Kooijman, E., Schmitt, M., Berndt, J., 2020. Initial 87Sr/86Sr as a sensitive tracer of Archaean crust-mantle evolution: Constraints from igneous and sedimentary rocks in the western Dharwar Craton. *India. Precambrian Research* 337, 105523.
- Roeder, P.L., MacArthur, D., Ma, X.P., Palmer, G.R., Mariano, A.N., 1987. Cathodoluminescence and microprobe study of rare-earth elements in apatite. *Am. Mineral.* 72, 801–811.
- Schmidt, K., Garbe-Schönberg, D., Bau, M., Koschinsky, A., 2010. Rare earth element distribution in >400 C hot hydrothermal fluids from 5 S, MAR: The role of anhydrite in controlling highly variable distribution patterns. *Geochim. Cosmochim. Acta* 74, 4058–4077.
- Shields, G., Stille, P., 2001. Diagenetic constraints on the use of cerium anomalies as palaeoseawater redox proxies: an isotopic and REE study of Cambrian phosphorites. *Chem. Geol.* 175 (1–2), 29–48.
- Stanley, J.K., Byrne, R.H., 1990. The influence of solution chemistry on REE uptake by *Ulva lactuca* L. in seawater. *Geochim. Cosmochim. Acta* 54 (6), 1587–1595.
- Steiner, M., Wallis, E., Erdtmann, B.-D., Zhao, Y., Yang, R., 2001. Submarine-hydrothermal exhalative ore layers in black shales from South China and associated fossils—insights into a Lower Cambrian facies and bio-evolution. *Palaeogeogr. Palaeoclimatol. Palaeoecol.* 169 (3–4), 165–191.
- Stormer, J.C., Pierson, M.L., Tacker, R.C., 1993. Variation of F and Cl X-ray intensity due to anisotropic diffusion in apatite during electron microprobe analysis. *Am. Mineral.* 78, 641–648.
- Tillberg, M., Maskenskaya, O.M., Drake, H., Hogmalm, J.K., Broman, C., Fallick, A.E., Åström, M.E., 2019. Fractionation of Rare Earth Elements in Greisen and Hydrothermal Veins Related to A-Type Magmatism. *Geofluids* 2019, 1–20.
- Trappe, J., 2006. Phanerozoic phosphorite depositional systems: a dynamic model for a sedimentary resource system, 76. Springer.
- Veizer, J., Ala, D., Azmy, K., Bruckschen, P., Buhl, D., Bruhn, F., Carden, G.A.F., Diener, A., Ebneth, S., Godderis, Y., Jasper, T., Korte, C., Pawellek, F., Podlaha, O.G., Strauss, H., 1999. ⁸⁷Sr/⁸⁶Sr, ^δ¹³C and ^δ¹⁸O evolution of Phanerozoic seawater. *Chem. Geol.* 161 (1–3), 59–88.
- Villaseca, C., García Serrano, J., Orejana, D., 2020. Pyroxenites and Megacrysts From Alkaline Melts of the Calatrava Volcanic Field (Central Spain): Inferences From Trace Element Geochemistry and Sr–Nd Isotope Composition. *Front. Earth Sci.* 8, 132.
- Von Damm, K.L., 1990. Seafloor hydrothermal activity: black smoker chemistry and chimneys. *Annu. Rev. Earth Planet. Sci.* 18 (1), 173–204.
- Wang, X.C., Li, X.H., Li, W.X., Li, Z.X., 2007. Ca. 825 Ma komatiitic basalts in South China: First evidence for > 1500 C mantle melts by a Rodinian mantle plume. *Geology*, 35(12), 1103–1106. Wheat, C.G., Feely, R.A., & Mottl, M.J. (1996). Phosphate removal by oceanic hydrothermal processes: An update of the phosphorus budget in the oceans. *Geochim. Cosmochim. Acta* 60, 3593–3608.
- Wilby, P.R., Briggs, D.E., Bernier, P., Gaillard, C., 1996. Role of microbial mats in the fossilization of soft tissues. *Geology* 24, 787–790.

- Woodhead, J.D., Hergt, J.M., 2001. Strontium, neodymium and lead isotope analyses of NIST glass certified reference materials: SRM 610, 612, 614. *Geostandard Newsletter* 25, 261–266.
- Xia, F., Ma, D., Pan, J., Sun, Z., Cao, S., Nie, W., Wu, K., 2004. Strontium isotopic signature of hydrothermal sedimentation from Early Cambrian barite deposits in east Guizhou, China. *Chinese Science Bulletin* 49 (24), 2632–2636.
- Xin, H., Jiang, S.Y., Yang, J.H., Wu, H.P., Pi, D.H., 2015. Rare earth element and Sr–Nd isotope geochemistry of phosphatic rocks in Neoproterozoic Ediacaran Doushantuo Formation in Zhangcunping section from western Hubei Province, South China. *Palaeogeogr. Palaeoclimatol. Palaeoecol.* 440, 712–724.
- Xin, H., Jiang, S., Yang, J., Wu, H., Pi, D., 2016. Rare earth element geochemistry of phosphatic rocks in Neoproterozoic Ediacaran Doushantuo Formation in hushan section from the Yangtze Gorges area, South China. *J. Earth Sci.* 27 (2), 204–210.
- Xu, L., Lehmann, B., Mao, J., Nägler, T.F., Neubert, N., Böttcher, M.E., Escher, P., 2012. Mo isotope and trace element patterns of Lower Cambrian black shales in South China: multi-proxy constraints on the paleoenvironment. *Chem. Geol.* 318, 45–59.
- Xu, L., Lehmann, B., Mao, J., 2013. Seawater contribution to polymetallic Ni–Mo–PGE–Au mineralisation in Early Cambrian black shales of South China: evidence from Mo isotope, PGE, trace element, and REE geochemistry. *Ore Geol. Rev.* 52, 66–84.
- Xu, L., Lehmann, B., Mao, J., Wenjun, Q., Andao, D., 2011. Re–Os age of polymetallic Ni–Mo–PGE–Au mineralisation in Early Cambrian black shales of South China—a reassessment. *Econ. Geol.* 106, 511–522.
- Yang, J.H., Kang, L.F., Peng, J.T., Zhong, H., Gao, J.F., Liu, L., 2018. In-situ elemental and isotopic compositions of apatite and zircon from the Shuikoushan and Xihuashan granitic plutons: Implication for Jurassic granitoid-related Cu–Pb–Zn and W mineralisation in the Nanling Range, South China. *Ore Geol. Rev.* 93, 382–403.
- Ye, Y., Wang, H., Wang, X., Zhai, L., Wu, C., Zhang, S., 2020. Elemental geochemistry of lower Cambrian phosphate nodules in Guizhou Province, South China: An integrated study by LA-ICP-MS mapping and solution ICP-MS. *Palaeogeogr. Palaeoclimatol. Palaeoecol.* 538, 109459.
- Ye, Y.-T., Wang, H.-J., Wang, X.-M., Zhai, L.-N., Wu, C.-D., Zhang, S.-C., 2021. In-situ rare earth element analysis of a lower Cambrian phosphate nodule by LA-ICP-MS. *Geol. Mag.* 158 (4), 749–758.
- Yin, R., Xu, L., Lehmann, B., Lepak, R.F., Hurley, J.P., Mao, J., Feng, X., Hu, R., 2017. Anomalous mercury enrichment in Early Cambrian black shales of South China: mercury isotopes indicate a seawater source. *Chem. Geol.* 467, 159–167.
- Ying, Y.C., Chen, W., Simonetti, A., Jiang, S.Y., Zhao, K.D., 2020. Significance of hydrothermal reworking for REE mineralisation associated with carbonatite: Constraints from in-situ trace element and C–Sr isotope study of calcite and apatite from the Miaoya carbonatite complex (China). *Geochim. Cosmochim. Acta* 280, 340–359.
- Zack, T., Hogmalm, K.J., 2016. Laser ablation Rb/Sr dating by online chemical separation of Rb and Sr in an oxygen-filled reaction cell. *Chem. Geol.* 437, 120–133.
- Zeng, Z., Ma, Y., Yin, X., Selby, D., Kong, F., Chen, S., 2015. Factors affecting the rare earth element compositions in massive sulfides from deep-sea hydrothermal systems. *Geochem. Geophys. Geosyst.* 16 (8), 2679–2693.
- Zeng, L.P., Zhao, X.F., Li, X.C., Hu, H., McFarlane, C., 2016. In-situ elemental and isotopic analysis of fluorapatite from the Taocun magnetite-apatite deposit, Eastern China: Constraints on fluid metasomatism. *Am. Mineral.* 101, 2468–2483.
- Zhao, Z., Shen, B., Zhu, J.M., Lang, X., Wu, G., Tan, D., Ma, H., 2021. Active methanogenesis during the melting of Marinoan snowball Earth. *Nat. Commun.* 12 (1), 1–9.
- Zhao, X.F., Zhou, M.F., Gao, J.F., Li, X.C., Li, J.W., 2015. In-situ Sr isotope analysis of apatite by LA-MC-ICPMS: constraints on the evolution of ore fluids of the Yinachang Fe–Cu–REE deposit, Southwest China. *Miner. Deposita* 50, 871–884.
- Zheng, J., Griffin, W.L., O'Reilly, S.Y., Zhang, M., Pearson, N., Pan, Y., 2006. Widespread Archean basement beneath the Yangtze craton. *Geology*, 34(6), 417–420. Zhou, Y., Zhong, H., Li, C., Ripley, E.M., Zhu, W.G., Bai, Z.J., & Li, C. (2017). Geochronological and geochemical constraints on sulphide mineralisation in the Qingmingshan mafic intrusion in the western part of the Proterozoic Jiangnan orogenic belt along the southern margin of the Yangtze craton. *Ore Geol. Rev.* 90, 618–633.
- Zhu, B., Jiang, S.Y., Yang, J.H., Pi, D., Ling, H.F., Chen, Y.Q., 2014. Rare earth element and SrNd isotope geochemistry of phosphate nodules from the lower Cambrian Niutitang Formation, NW Hunan Province, South China. *Palaeogeogr. Palaeoclimatol. Palaeoecol.* 398, 132–143.
- Zhu, B.L., Jiang, S.Y., 2017. A LA-ICP-MS analysis of rare earth elements on phosphatic grains of the Ediacaran Doushantuo phosphorite at Weng'an, South China: implication for depositional conditions and diagenetic processes. *Geol. Mag.* 154 (6), 1381–1397.